1   **Experimental constraints on mantle sulfide melting up to 8 GPa (Revision 2)**

2   **ZHOU ZHANG[1,*] AND MARC M. HIRSCHMANN[1]**

3   [1]Department of Earth Sciences, University of Minnesota, Minneapolis, Minnesota 55414, U.S.A

4   * E-mail: zhan1721@umn.edu

5   **ABSTRACT**

6   We present high pressure experiments up to 8 GPa that constrain the solidus and liquidus of a

7   composition, $Fe_{0.69}Ni_{0.23}Cu_{0.01}S_{1.00}$, typical of upper mantle sulfide. Solidus and liquids brackets

8   of this monosulfide are parameterized according to a relation similar to the Simon-Glatzel

9   equation, yielding, respectively, $T(°C)=1015.1[P(GPa)/1.88+1]^{0.206}$ and

10   $T(°C)=1067.3[P(GPa)/1.19+1]^{0.149}$ ($1 \leq P \leq 8$). The solidus fit is accurate within ± 15 °C over the

11   pressure intervals 1-3.5 GPa and within ± 30 °C over the pressure intervals 3.5-8.0 GPa. The

12   solidus of the material examined is cooler than the geotherm for convecting mantle, but hotter

13   than typical continental geotherms, suggesting that sulfide is molten or partially molten through

14   much of the convecting upper mantle, but potentially solid in the continental mantle. However,

15   the material examined is one of the more refractory among the spectrum of natural mantle sulfide

16   compositions. This, together with the solidus-lowering effects of O and C not constrained by the

17   present experiments, indicates that the experimentally-derived melting curves are upper bounds

18   on sulfide melting in the Earth's upper mantle and that the regions where sulfide is molten are

19   likely extensive in both the convecting upper mantle and, potentially, the deeper parts of the

20   oceanic and continental lithosphere, including common source regions of many diamonds.

21   **Keywords:** Sulfide, mantle, solidus, melting, experimental constraint, calibration

INTRODUCTION

23 Molten sulfides are important geochemical and geophysical agents in Earth's interior. Sulfide

24 mineral and melt are the chief carriers of siderophile and chalcophile elements in the upper

25 mantle (Pearson et al. 2003) and mobilization of sulfide melts may produce fractionated

26 chalcophile and platinum group element (PGE) patterns (Alard et al. 2000, 2002; Ballhaus et al.

27 2006; Bockrath et al. 2004; Delpech et al. 2012; Hart and Gaetani 2006; Li and Audétat 2012;

28 Powell and O'Reilly 2007). Furthermore, sulfides are key hosts of Os, Pb, and potentially He and

29 therefore play an important role in evolution of important isotopic systems (Hart and Gaetani

30 2006; Huang et al. 2014; Pearson et al. 2002; Roy-Barman et al. 1998). Consequently, they are

31 widely-used targets for Re-Os and Pb-Pb geochronologic studies (Pearson et al. 1998, 2003) but

32 interpretation of resulting ages depends on sulfide parageneses. Sulfide melts are also potentially

33 responsible for mantle geophysical anomalies, as their physical properties differ greatly from

34 those of silicates. These include higher density, surface tension, electrical conductivity and lower

35 melting points (Bockrath et al. 2004; Helffrich et al. 2011; Mungall and Su 2005). For example,

36 it has been speculated that sulfide melts are responsible for seismic anomalies at ~100 km in

37 continental cratons (Helffrich et al. 2011).

38 A key feature of natural sulfide is that it may be molten in large parts of the mantle (e.g.,

39 Bockrath et al. 2004; Hart and Gaetani 2006) and so constraining its geochemical and

40 geophysical role requires defining the conditions of sulfide melt stability. Although detailed one

41 atmosphere studies have explored the Fe-Ni-S phase diagrams at 900 °C-1350 °C (e.g., Hseih et

42 al. 1987; Waldner and Pelton 2004 and references therein), the majority of high pressures studies

43 on sulfide melting to date have been performed on simple stoichiometric or eutectic

44 compositions (Boehler 1992, 1996; Ryzhenko and Kennedy 1979; Sharp 1969; Usselman 1975).

45 Many of these have focused on the influence of sulfide on core formation, and so have examined

46 relations in metal-rich compositions, including studies to very high pressures (Boehler 1992; Fei

47 et al. 1997; Morard et al. 2011; Stewart et al. 2007). But fewer studies have considered melting

48 relations of compositions appropriate for the modern upper mantle, and these have been limited

49 to relatively low (≤ 3.5 GPa) pressures (Ballhaus et al. 2006; Bockrath et al. 2004).

50 Comparison of experimental studies of stoichiometric sulfides to those conducted in metal-rich

51 sulfide-metal eutectics shows that melting temperatures are strongly variable depending on

52 metal/sulfide ratios (Fig. 1). Further, substitution of Ni and Cu for Fe also influences melting

53 temperatures (Hseih et al. 1987; Urakawa et al. 1987). Consequently, understanding melting of

54 upper mantle sulfides requires perspective on the range of compositions likely to be present.

55 Compositions of natural mantle sulfides are quite variable, in part owing to their tendency to

56 exsolve on cooling (Pearson and Wittig 2014; Richardson et al. 2001). The most reliable records

57 derive from reintegrated compositions from inclusions in olivine or diamond, studies of which

58 (Aulbach et al. 2009; Westerlund et al. 2006) indicate that most upper mantle sulfides have

59 compositions close to monosulfide stoichiometry with metal/sulfide (M/S) ratios typically

60 between 0.9-1.2 (Fig. 2).

61 Previous experimental constraints on the high pressure melting of monosulfide similar to natural

62 mantle composition derive chiefly from the studies of Bockrath et al. (2004) and Ballhaus et al.

63 (2006). Bockrath et al. (2004) documented the melting interval of a bulk composition ⬚ with an

64 M/S ratio of 0.93, which is at the low end of the range present in natural mantle compositions

65 (Fig. 2a; Table 1). Ballhaus et al. (2006) reported further compositional details about the phases

66 produced by melting at ⬚ and extended this work to include two more metal-rich compositions,

67 ⬚ with M/S of 1.06 and ⬚ with M/S of 1.11. All three compositions had Ni contents (15.5 wt.%)

3

68   appropriate for mantle sulfides as calculated Fe-Ni exchange equilibrium with mantle olivine,

69   and small amounts of Cu. The solidus of the low M/S □ is near 1075°C at 0.1 MPa and 1275 °C

70   near 3 GPa, placing it below the convecting mantle adiabat (Katsura et al. 2010), above typical

71   continental geotherms (Pollack and Chapman 1977), and similar to temperatures for

72   intermediate-age oceanic lithosphere (Turcotte and Schubert 2002). More metal rich

73   compositions □ and □ have markedly lower solidi: that of □ is 75-100 °C lower than for □. The

74   solidus of □ appears to be as low as 800 °C and with very little pressure dependence, perhaps

75   because its composition falls outside of the field for mss (Fig. 2b). It likely has more than one

76   phase below the solidus and so its melting behavior is similar to that at the Fe-FeS or (Fe,Ni)S-

77   (Fe,Ni)O eutectics (Fig. 1).

78   Together, these data indicate that mantle sulfide is partially molten in the hotter parts of the

79   upper mantle, but significant questions remain. The experiments on natural monosulfide (mss)

80   compositions extend only to 3.5 GPa and so do not pertain to the deeper parts of continental

81   lithosphere or the oceanic low velocity zone. Also, constraints on the liquidus are absent for □

82   and □ and produce curious results for □, indicating a concave upward trend that is contrary to

83   expected melting behavior (e.g., Hart and Gaetani 2006). Here we present partial melting

84   experiments on a bulk composition similar to □ up to 8 GPa. Our purpose is to verify the solidus

85   and liquidus determined by Bockrath et al. (2004), and to determine the phase relations of this

86   relatively refractory composition to higher pressure. An additional motivation is to refine

87   pressure and temperature calibrations in the piston cylinder and multi-anvil devices, to enhance

88   the reliability of the sulfide melting results.

89

EXPERIMENTAL METHODS

90

Starting materials and preparation of sample capsules

91

92   Experimental starting materials were prepared by mixing Alfa-Aesar reagents including Fe (99.9%

93   powder), FeS_2 (99.9% powder), Ni (99.8% powder) and Cu (99.9% powder). The mixture was

94   homogenized by grinding under ethanol in an agate mortar for 1 hour. After mixing, samples

95   were dried at 110 °C in a vacuum oven for 5 minutes. Subsequently, starting mixes were stored

96   in a sealed glass container in a sealed glass desiccator to avoid oxidation. Subsequent electron

97   microprobe analysis of post-experiment samples indicate <0.6 wt.% oxygen, suggesting minimal

98   oxidation of the starting material.

99   Starting mixtures were loaded into silica glass capsules, which consisted of a tube closed with a

100   cap on both ends. For piston cylinder experiments, tubes were 2 mm long with inner and outer

101   diameters of 2 and 3 mm and the caps were each 1 mm long. For multi-anvil experiments, the

102   tubes were 1 mm long, with inner and outer diameters of 1 and 2 mm, and caps were 1 mm long.

High-pressure experiments

103

104   Experiments were performed using an end-loaded piston cylinder (PC) device and a 1000-ton

105   Walker-style multi-anvil (MA) apparatus using procedures described in detail by Xirouchakis et

106   al. (2001) and Dasgupta et al. (2004). The PC experiments were conducted in 1.27 cm diameter

107   pressure vessels from 0.8-3.3 GPa using a hot piston in technique, with hydraulic pressure

108   maintained constant during the run period and with temperature controlled by a type B ($Pt_{70}Rh_{30}/$

109   $Pt_{94}Rh_6$) thermocouple located 1 mm above the top of the capsule. Assemblies consisted of

110   $BaCO_3$ cells with MgO spacers and a graphite heater. MgO assemblies were dried at 1000 °C for

111 8-15 hours and stored in a drying oven at 110 °C. The MA experiments were conducted at 2.7-

112 8.0 GPa using 18/12 OEL/TEL assemblies, including cast MgO-Al_2O_3-SiO_2-Cr_2O_3 octahedra and

113 integrated gasket fins. Straight-walled graphite furnaces and type C ($W_{74}Re_{26}/W_{95}Re_5$)

114 thermocouples were used for all MA experiments and are located ~1 mm from the sulfide

115 charges. Samples were compressed to target pressures, dwelling for 5 hours to allow assembly

116 stabilization and then heated to the target temperature. Both PC and MA experiments were

117 quenched by power termination. Individual experimental run conditions are detailed in Table 3.

118 **Pressure and temperature calibration experiments**

119 To ensure that experimental temperatures and pressures were accurate for the conditions of the

120 sulfide melting experiments, we conducted several new calibrations to refine previous

121 documentation of PC and MA performance in the UMN experimental petrology laboratory by

122 Xirouchakis et al. (2001), Dasgupta et al. (2004), Withers et al. (2011) and Tenner et al. (2012).

123 Pressure calibrations were conducted against the quartz-coesite transition (Bohlen and Boettcher

124 1982; Bose and Ganguly 1995). Temperature calibration was conducted against the melting

125 temperature of Au (Mirwald and Kennedy 1979).

126 For quartz-coesite experiments in the PC device, a homogeneous mixture of the two phases

127 (50:50) was sealed in Pt capsules. The quartz was taken from a crushed natural gem-quality

128 crystal. The coesite was presynthesized from Corning silica glass in a graphite capsule at 900 °C

129 and 4 GPa, based on previous syntheses conducted by Luo et al. 2002, and verified by XRD.

130 Each experiment lasted 2 to 12 hours at the target temperature and pressure and then the Pt

131 capsule was cut and the portion of the post-run product that had been closest to the thermocouple

132 was collected for XRD analysis. Because reaction was not always complete, the intensities of the

6

133 XRD peaks of experimental samples were compared to those of the starting mixture. In the MA

134 apparatus, the silica glass capsule sample lids from sulfide melting experiments were examined

135 post-experiment. The top lid of the silica capsule was recovered and analyzed by Raman

136 Spectroscopy and ground to a powder for XRD.

137 For the Au melting experiments, a 2-mm diameter and 2-mm length hole was drilled into the

138 MgO spacers in the same geometry as the capsule would residue during a normal experiment,

139 and the hole was filled with NaCl powder into which an Au wire was placed. The sample was

140 heated to 30 °C below the target temperature and held for 2 hours to ensure pressure stabilization.

141 After that, temperature increased by 10 °C/min to the target temperature. The experiment was

142 held at the target temperature and pressure for 6 minutes and was then quenched to room

143 temperature. The post-run sample was placed in a beaker filled with water, thereby dissolving the

144 NaCl. Au spheroids indicated melting whereas relict wires remained in subsolidus melting

145 experiments (Fig. 3).

146 **Analytical methods**

147 Following sulfide melting experiments, the assembly was gradually decompressed to minimize

148 sample fracturing and the recovered capsules were mounted in epoxy and ground to expose the

149 medial section of the charges. Owing to the low hardness of sulfide, the sample was impregnated

150 with epoxy prior to grinding. Polishing was conducted with diamond polishing pads, starting

151 from 9.0-micrometer grit down to 0.5-micrometer. Run products and standards were carbon

152 coated and analyzed using a JEOL JXA8900R electron microprobe by WDS analyses with an

153 accelerating voltage of 15 kV and a probe current of 20 nA. Counting times were 20 s on peak

154 centroid and 10 s on each background for all elements. Oxygen was measured using a multilayer

7

155   crystal (LDE2 with 2d = 9.7nm). Primary standards used for major elements analysis were pyrite

156   (FeS$_2$) for Fe and S, Ni metal for (Ni), chalcocite (Cu$_2$S) for Cu and S, and magnetite (Fe$_3$O$_4$) for

157   O. Troilite was used as a secondary standard for Fe and S. Pyrite was used as a blank for oxygen.

158   We employed a focused beam on crystalline sulfides and a defocused beam (1-20 micron

159   diameter) on quenched melts.

RESULTS AND DISCUSSION

161   **Pressure and temperature calibration**

162   Comparison of the quartz-coesite reaction at 1100 °C bracketed by the PC with the reaction

163   determined by Bohlen and Boettcher (1982) and Bose and Ganguly (1995) suggests a pressure

164   correction of -0.4 GPa (Table 2). For the MA, the coesite-quartz bracket 1230-1250 °C in this

165   study falls between the previously-determined force-pressure curves determined at low

166   temperature (1000-1200 °C, Dasgupta et al. 2004), and high temperature (1440-1700 °C,

167   unpublished data) (Fig. 4a) and suggests a similar force-pressure relationship to that from

168   enstatite-pyrope experiments in the same assembly at 1300-1400 °C (Tenner et al. 2012).

169   Because the high temperature and low temperature F-P curves converge at high pressure, the

170   intermediate temperature quartz-coesite and enstatite-pyrope brackets can be used to construct a

171   force-pressure calibration curve valid from 3 to 8 GPa (Fig. 4a).

172   Comparison of gold melting experiments to the Au fusion curve of Mirwald et al. (1975) and

173   Mirwald and Kennedy (1979) indicate that sample temperatures are 10-15 and 15-20 °C hotter

174   than thermocouple readings for the PC and MA assemblies, respectively. The former is in good

175   agreement with the 12 °C offset determined in the PC from multiple thermocouple measurements

176   (Xirouchakis et al. 2001) and the latter is similar to that estimated by previous studies in the MA

177   (Dasgupta et al. 2004; Withers and Hirschmann, 2007; Tenner et al. 2012). All sulfide melting

178   temperatures and pressures reported in Table 1 have been adjusted for the pressure and

179   temperature calibrations reported here.

180   The pressure calibration determined for the $BaCO_3$ assemblies in the PC at 1100 °C suggest a

181   friction correction of -12%, which is nearly twice to that determined at comparable pressures in

182   the same assembly in the UMN laboratory at 1250 °C based on the anorthite breakdown reaction

183   (Xirouchakis et al. 2001). The difference is presumably owing to greater friction at lower

184   temperature. Previous studies for $BaCO_3$ assemblies at comparable pressures have found similar

185   friction corrections (15% Fram and Longhi 1992; 9% McDade et al. 2002). In contrast to results

186   in the UMN laboratory, McDade et al. (2002) found friction in the $BaCO_3$ pressure assembly to

187   be independent of temperature from 1000-1600 °C. It remains unclear whether differences in

188   calibration are owing to subtle differences in assemblies or piston cylinder performance, but

189   comparison between different calibrations suggest that interlaboratory pressure accuracies for PC

190   experiments are, in best cases, ±0.1 GPa.

191   **Phase relations, solidus, and liquidus determinations**

192   Phase relations were determined chiefly from textural and compositional observations based on

193   optical backscattered electron (BSE) images (Fig. 5) and electron microprobe analyses (Table 3)

194   Combining both textures and compositions, phase relations are determined on melt and mss. On

195   the one hand, textures of mss and melt are different based on the observation of optical images

196   and backscattered electron (BSE) images. Mss in the post-run charge is homogenous granular

197   grains in texture; melt was quenched into crystals with a wormlike intergrowth texture. On the

198   other hand, Cu, Ni, Fe and S are fractionated between melt and mss if both phases coexist and

9

199   equilibrate at high temperature before quenching, with Cu and Ni being incompatible in the Fe-

200   Ni-Cu-S monosulfide system (discussion in the next section below). In addition, mss phases are

201   homogenous by composition at micron scale while quenched melts are highly heterogeneous by

202   composition at micron scale. This is the reason for the employment of a focused beam on

203   crystalline sulfides and a defocused beam (1-20 micron diameter) on quenched melts. From the

204   perspective of polishing, due to the hardness contrast between quartz and sulfide, post-run

205   products were polished with prevalent cracks on the surface. During polishing, subsolidus

206   aggregates tend to disintegrate whereas superliquidus and partially melted experiments do not

207   tend to disintegrate.

208   Exposed charges were unavoidably pervasively cracked during polishing, owing to the hardness

209   contrast between sulfide charges and surrounding silica minerals. In some cases, this prevented

210   high quality polishes across the entire charge, but sufficient material was always exposed to

211   allow textural and compositional analysis. Selected BSE images are shown in Fig. 5 and electron

212   microprobe analyses are reported in Table 3. The subsolidus samples consist of a homogeneous

213   single monosulfide (mss) phase with granular texture and grain diameters typically 100-300

214   microns (Fig. 5a) with a composition that in all cases is within analytical uncertainty of the

215   starting material (Fig. 5a). Experiments that underwent partial melting produced two phases (Fig.

216   5b): a homogenous Fe-rich mss phase granular mss crystals typically > 100 microns and a Ni-Cu

217   rich heterogeneous phase material that, following quench, consists of smaller (50 micron) grains

218   interspersed with darker (on BSE) with wormlike intergrowths between grains textures. Crystals

219   and quenched melt are well-segregated by gravity. Electron microprobe analyses indicate

220   compositions that are more heterogeneous than subsolidus mss, but the bulk compositions are

221   comparable to that of the starting composition (Fig. 5b). Experiments inferred to have been

10

222   superliquidus quench to textures consisting of two sulfide phases in a wormlike intergrowth,

223   similar to those produce by partially molten samples with the same composition as the starting

224   material within starting powder mixing uncertainty and analytical uncertainty (Fig. 5c).

225   Additional textural evidence that aided the interpretation of solidus location was the behavior

226   during polishing: subsolidus aggregates tended to disintegrate, whereas superliquidus and

227   partially melted experiments were more cohesive.

228   Crystalline mss produced in subsolidus experiments are compositionally homogeneous within

229   analytical uncertainty and are not distinguishable from the bulk composition (Table 3). When

230   melt and crystals coexist at high temperature, granular sulfides are compositionally

231   homogeneous and enriched in Fe and S and poor in Ni and Cu relative to the bulk composition.

232   In comparison, the quenched melt phase is heterogeneous on a micron scale, necessitating

233   analysis with an unfocussed electron beam. The quenched melt phase is depleted in Fe and S and

234   enriched in Ni and Cu relative to the crystalline solids or the bulk composition. In one case

235   (Experiment M794, 6.9 GPa, 1400 °C), quenched melt was observed but coexisting granular

236   crystals were not evident. However, sub-liquidus conditions were inferred because the melt

237   composition was enriched in Cu and Ni relative to the bulk composition. Melts interpreted to be

238   quenched from superliquidus conditions based on textural features are also heterogeneous, but

239   have compositions within analytical uncertainty of the starting composition.

240   Experimental determinations of the mss solidus and liquidus up to 8 GPa can be fit with an

241   empirical relation that minimizes the disagreement between observations and the computed

242   curve according to a penalty function as described by Hirschmann (2000), for which an objective

243   variable, Y, given by $Y = \Sigma (T_i)^2$, is minimized, where T_i is given by

11

T_i $= (T_i\text{-}T_{model})^2$;   if the assemblage observed at T_i disagrees with T_{model}

$=0$;   if the assemblage observed at T_i agrees with T_{model}

244   and T_{model} is the temperature calculated from the solidus or liquidus curve. We examined several

245   types of functions to fit to the solidus and liquidus brackets, including polynomial and

246   logarithmic forms, and though the differences among these fits are small, ultimately chose to

247   employ an equation similar to that proposed by Simon and Glatzel (1929),

248   $$T = T_{ref}\left(\frac{P}{a}+1\right)^c$$

249   where T is temperature (°C) and P is pressure (GPa). For the solidus up to 8 GPa, we find T_{ref}

250   $=1015.1$°C, $a=1.88$, and $c=0.206$ ($0{\leq}P{\leq}8$) (Y=768), and, for the liquidus, $T_{ref}=1067.3$ °C, $a=1.19$

251   and c=0.149 (Fig. 6).

252   In this study, the solidus fit $T(°C)=1015.1[P(GPa)/1.88+1]^{0.206}$, is thought to be accurate within $\pm$

253   15 °C over the pressure interval from 1 to 3.5 GPa and within $\pm$ 30 °C from 3.5 to 8.0 GPa,

254   owing to different temperature uncertainties in PC and MA devices and different *P-T* densities of

255   experimental brackets (typically 25 °C for PC and 50 °C for MA experiments). The fit from 0.1

256   MPa to 0.8 GPa might be less accurate because brackets constraining solidus at 0.1 MPa were

257   taken from previous studies and the present study included no experiments between 0.1 MPa-0.8

258   GPa. Therefore, this solidus is constrained chiefly to mantle depths of 30 km to 250 km.

259   At high pressures, the solidus and liquidus curves tend to converge, producing a narrowed

260   melting interval. This may be an artifact of imperfections in the regressed curves, with the

261   Simons equation predicting solidus temperatures that are near the high limit of the experimental

262   brackets, and the liquidus curve poorly constrained owing to few high pressure observations.

263   The melting interval for mss can be compared to that determined by Bockrath et al. 2004 for an

264   apparently identical composition in similar capsules up to 3.5 GPa (Fig. 7). Solidus temperatures

265   are consistent, but the liquidus found by Bockrath et al. 2004 extends to much higher

266   temperature – e.g., at 3 GPa Bockrath et al. (2004) observed mss coexisting with melt up to

267   1400 °C, but the new results place the liquidus near 1275 °C. As noted by Hart and Gaetani

268   (2006), the high melting temperatures indicated by Bockrath et al.'s experiments suggest a

269   concave upward liquidus slope and, at pressures near 3 GPa, liquidus temperatures hotter than

270   the melting of pure $Fe_{1-x}S$ (Ryzhenko and Kennedy 1973) (Fig. 1), both of which are unlikely.

271   These inconsistencies are absent from the new liquidus curve.

272   The melting interval for mss determined in this study is intermediate between the high

273   temperature fusion curves of pure troilite, FeS, or pyrrhotite, $Fe_{1-x}S$, and eutectic melting in the

274   system FeS-Fe (Fig. 1). The pyrrhotite studied by Ryzhenko and Kennedy (1973) had similar

275   metal/sulfide stoichiometry to the mss studied here (Table 1), meaning that the lower melting

276   temperature of the mss is owing chiefly to the effects of Fe-Ni solid solution. This is consistent

277   with many previous studies that have found that Ni reduces the melting temperature of

278   monosulfide (Hsieh et al. 1987; Urakawa 1987).

279   **Partial melting and fractionation of elements between melt/mss**

280   For experiments that produce coexisting melt and monosulfide crystals, melt fractions calculated

281   independently from Fe and Ni mass balance (Table 2) agree well with one another (Fig. 8). Melt

282   fractions calculated from Ni are considered most accurate because of the strong mineral/melt

283   partitioning and high concentrations (compared to Cu) produce phase compositions that are most

284   strongly separated compared to analytical uncertainties. Therefore, Ni concentration in melts is

13

285   chosen to represent melt evolution. In all samples, the melts have slightly higher metal/sulfur

286   ratio than their coexisting residue mss (Table 3). Ni and Cu preferentially partition into melts and

287   Fe is concentrated in residue mss (Fig. 9). The detection limit for oxygen established by

288   analyzing pyrite is ~0.05 wt.%, with the analytical uncertainty of ±0.1 wt.%. Oxygen is detected

289   in small amounts in both mss and melt. Oxygen concentrations in the post-run products vary

290   from 0.2-0.6 wt.%, with slightly greater concentrations in quenched melts compared to crystals

291   (Table 3). The concentrations detected in our study are comparable to those (~0.37 wt.%) found

292   previously in pyrrhotite annealed at 700 °C (Graham et al. 1987; Graham and McKenzie 1987).

293   Partial melt compositions have higher M/S ratios than residual mss solids (Table 3), consistent

294   with relations established previously for melting of mss (Kullerud 1963; Bockrath et al. 2004;

295   Ballhaus et al. 2006) and in simple systems (Ryzhenko and Kennedy 1973). MSS compositions

296   change comparatively little, being restricted chiefly to M/S ratios between 0.90-0.93 owing

297   chiefly to the constraints of M/S stoichiometry in mss solid solutions (Ballhaus et al. 2006),

298   whereas melt compositions are more variable (M/S=0.94-1.02). Partial melts are also enriched in

299   Ni and especially Cu compared to coexisting mss, whilst Fe concentrations are similar in the two

300   phases. This is as expected owing to the respective radii of the cations (Cu>Ni>Fe). Mineral/melt

301   partition coefficients for Cu and Ni become more extreme at low melt fractions, likely owing to

302   the increased Ni/(Fe+Ni) of the melts (Fig. 9). Based on the enrichment or depletion of Cu and

303   Ni, sulfides from mantle xenoliths or diamond inclusions has been interpreted as either trapped

304   melts or residual mss crystals (Bulanova et al. 1996; Guo et al. 1999; Lorand and Alard 2001).

305   Such interpretations are broadly consistent with the experimental compositions observed here.

306   The variations in metal/silicate and Cu-Ni-Fe fractionations with melt fraction and temperature

307   are linked to the constraints on mss stoichiometry and the influence of Ni on partitioning

14

308   behavior. These relationships vary only weakly with pressure, as has been previously

309   documented for M/S partitioning (Ballhaus et al. 2006) and Ni partitioning (Jones and Walker

310   1991). The lack of pressure influence on partitioning suggests that the melting interval between

311   solidus and liquidus curves should not become significantly wider or narrower with pressure, and

312   reinforces the assertion above that the liquidus, which is under-constrained at pressures above

313   3.5 GPa, likely is slightly hotter at high pressure than indicated by the parameterization.

314   **Sulfide composition in the mantle**

315   The sulfide solidus is affected by composition, which in the mantle, is controlled by reactions

316   between sulfides and coexisting silicate minerals (Eggler and Lorand, 1993; Gaetani and Grove,

317   1997). Solidus temperatures are lower when sulfide has higher M/S ratios (e.g. Ballhaus et al.

318   2006), and when additional components (such as C or O) are soluble (Ballhaus et al. 2006; Chi et

319   al. 2014; Dasgupta et al 2009; Gunn and Luth 2006; Urakawa et al 1987). The sulfide M/S (0.93)

320   investigated in this study is on the low end of natural mss (0.9-1.1) (Fig. 2), with low content of

321   oxygen and nominally carbon-free.

322   In the shallow oxidized mantle, oxygen dissolved in sulfide might be high (Gataeni and Grove

323   1999) and drive the sulfide solidus downward (Gunn and Luth 2006; Urakawa et al 1987). As the

324   mantle becomes more reduced with increasing depth (Frost and McCammon 2008), the oxygen

325   content should diminish, but this can be countered by increases in the M/S ratio owing to an

326   increase in metal activity, as the reactions

327   Fe_2SiO_4 (ol) = $FeSiO_3$ (opx) + ½ O_2 + Fe (sulfide)

328   Ni_2SiO_4 (ol) = $NiSiO_3$ (opx) + ½ O_2 + Ni (sulfide)

15
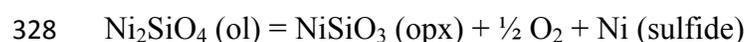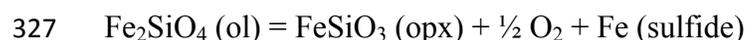
329   shift to the right. Equivalently, Eggler and Lorand (1993) suggest that oxygen fugacity (f_{O2}) and

330   sulfur fugacity (f_{S2}) are positively correlated for peridotite-sulfide systems. Reactions similar to:

331   Fe_2SiO_4 (ol) + ½ S_2 = $FeSiO_3$ (opx) + FeS (sulfide) + ½ O_2

332   also produce increases in M/S ratio of the sulfide as oxygen fugacity decreases. Furthermore, as

333   mantle enters the graphite/diamond stability field (>4 GPa) (Frost and McCammon, 2008),

334   dissolved carbon will likely further depress sulfide solidus temperatures.

335   All of these considerations together suggest that the sulfide solidus constrained in this study is

336   near an upper bound. At low pressures and more oxidized conditions, the solidus would be

337   lowered by greater dissolved oxygen, and at higher pressures and more reduced conditions, it

338   would be diminished by higher M/S ratio and dissolved C.

339   **Sulfide melts in the mantle**

340   The solidus and liquidus of monosulfide constructed from this study is below the calculated

341   mantle adiabat (Katsura et al. 2010) up to the limit of the experimental data at 8 GPa (Fig. 10),

342   meaning that sulfide is molten in the convecting mantle at least to depths of 250 km. We note

343   that the composition investigated has comparatively low M/S ratio, and that sulfides with higher

344   ratios melt at lower temperature (e.g. Ballhaus et al. 2006), so that melting is expected for most

345   or all mantle sulfide compositions. The steeper temperature/pressure slope of the melting curves

346   compared to the adiabat may indicate that sulfide becomes crystalline deeper in the mantle.

347   Increased M/S should in turn decrease the sulfide crystallization temperature (e.g. Ballhaus et al.

348   2006). If conditions at depth become sufficiently reducing such that a metal alloy phase is

349   stabilized (Frost et al. 2004; Rohrbach et al. 2007, 2011), then sulfide melting is controlled by

16

350   the (Fe,Ni)S-(Fe,Ni) eutectic, which remains below the adiabat at least until pressures reached

351   deep in the lower mantle (>60 GPa; Campbell et al. 2007; Morard et al. 2011; Stewart et al.

352   2007). Thus, sulfide melt may in fact be stable throughout the convecting upper mantle and

353   perhaps into the transition zone.

354   The sulfide melting curves intersects geotherms for typical oceanic lithosphere shallower than

355   the intersection with the adiabat, meaning sulfide could be partially molten in the thermal

356   boundary layer and deeper portions of the oceanic lithosphere (Fig. 10). In the continental

357   lithosphere, sulfides are less likely molten in the colder settings such as the root of cratons. Of

358   course, sulfides with higher M/S ratios and dissolved carbon could become molten at lower

359   temperatures.

360   **Sulfide inclusions in diamond**

361   Sulfide inclusions are abundant in diamond, and are typically Ni-rich (22 wt.%-36 wt.%) in

362   peridotitic parageneses (age >3 Ga) and Ni-poor (0-12 wt.%) in eclogitic diamonds (age <3 Ga),

363   which corresponds to high bulk Ni contents (~3000 ppm) in peridotite or and low bulk Ni (~300

364   ppm) concentrations typically found in eclogite (Bulanova et al. 1996; Pearson et al. 2003;

365   Shirey and Richardson 2011; Stachel and Harris 2008). The overabundance of sulfide in

366   diamond suggests that sulfide acts either as a reducing reagent or as a co-precipitating product

367   during diamond formation, more than likely as a liquid phase (Bulanova 1995; Stachel and

368   Harris 2008; Westerlund et al. 2006). Although the solidus of monosulfide investigated here is

369   hotter than typical diamond P-T, molten sulfide could be trapped in diamond if it originates from

370   compositions with comparatively high M/S ratios, or if additional components (such as C or O)

371   lower the solidus (Ballhaus et al. 2006; Gunn and Luth 2006). In addition, for sulfides that were

17

372   trapped as inclusions in large melt extraction process from peridotite, sulfides might be molten

373   due to this high temperature process in the earlier geological history. This is indicated by the

374   mantle sulfides Re-Os modal age peaks of 1.2, 1.9, and 2.7 billion years which match similar

375   periods of high tectonic activity recorded in zircon populations (Pearson et al. 2007). If sulfides

376   are trapped as liquids, then they are syngenetic with their hosts and geochronologic

377   interpretations of their Re-Os or Pb-Pb isotope systematics can be related to the timing of the

378   formation of the enclosing minerals.

379   **Mobility of sulfide melts**

380   Having established that sulfide is molten or partially molten in significant portions of the mantle,

381   a natural question is whether such melts are mobile. Sulfide melt mobility is affected by oxygen

382   fugacity and pressure in the mantle (Gaetani and Grove, 1999; Shannon and Agee 1998; Shi et al.

383   2013). At conditions similar to the fayalite-magnetite-quartz oxygen buffer, molten sulfide may

384   potentially dissolve up to 9 wt.% oxygen (Gaetani and Grove, 1999) and sulfide melt can

385   potentially form an interconnected network along silicate grain edges, as the olivine–melt

386   dihedral angle is 52° (Gaetani and Grove, 1999). As conditions become more reduced and

387   dissolved oxygen diminishes, the dihedral angle increases (e.g., 90° at near the iron-wüstite

388   buffer, Gaetani and Grove 1999) and interconnectivity is less likely. At lower mantle conditions,

389   where the principle silicate is perovskite rather than olivine, high dihedral angles for Fe-Ni-S

390   melts prevail (Shannon and Agee 1998; Shi et al. 2013), inhibiting connectivity. Therefore, in the

391   shallow mantle (e.g. 30-60 km), sulfide melts, if stable, potentially form an interconnected

392   network in olivine-rich rocks. In the deep lithosphere (e.g. >120 km), percolation may be limited

393   as conditions become more reduced (Frost and McCammon, 2008). Additionally, sulfide melt

394   transport may be coupled to movement of associated silicate or carbonate melts (Delpech et al.

395   2012; Lorand et al. 2004). In some cases, natural peridotite textures indicate sulfide wetting

396   silicate grain boundaries (Lorand et al. 2013). Furthermore, geochemical variations observed in

397   xenoliths may not be easily explicable without sulfide mass transport (Lorand 1989; Lorand et al.

398   2013).

399   Sulfide melt mobility may be a key factor determining their geophysical and geochemical

400   influence. For example, despite molten sulfide's extreme physical properties relative to silicate

401   rock, it may not impart significant geophysical anomalies simply by melting *in situ*, as the melt

402   fraction for rocks with typical mantle S concentrations (200 ppm, McDonough and Sun 1995)

403   would be merely 0.05-0.10 vol.%. If sulfide melts can migrate and concentrate in isolated areas,

404   they may feasibly produce noticeable effects on shear wave velocities (e.g., Helffrich et al. 2011)

405   and other properties. Likewise, sulfide melts are most likely to be responsible for geochemical

406   variations in chalcophile or PGE elements (e.g., Alard et al. 2002; Powell and O'Reilly 2007) if

407   they are mobile.

408   **IMPLICATIONS**

409   We   emphasize   that   we   have   investigated   only   a   single   composition   of   sulfide

410    $Fe_{0.69}Ni_{0.23}Cu_{0.01}S_{1.00}$ (M/S=0.93), which is calculated as in equilibrium with mantle olivine at

411   FMQ, with trace amounts of oxygen (and likely carbon). As the upper mantle becomes more

412   reduced with depth (Frost and McCammon, 2008), the M/S ratio of sulfide should increase,

413   leading to further depression of the sulfide solidus (Ballhaus et al. 2006; Rohrbach et al. 2007).

414   Also, in the oxidized shallow mantle (e.g. < 3 GPa), sulfides melts should have higher content of

415   oxygen and in the graphite/diamond stability field (e.g. > 4 GPa), dissolved carbon should

416   increase, and both of these should affect melting temperatures. Therefore, the solidus constrained

417   in this work is likely an upper bound on sulfide melting in the Earth's upper mantle.

418   **ACKNOWLEDGEMENTS**

424

425   **REFERENCES CITED**

426   Alard, O., Griffin, W. L., Lorand, J. P., Jackson, S. E., and O'Reilly S. Y. (2000) Non-chondritic

427   distribution of the highly siderophile elements in mantle sulfides. Nature, 407, 891-894.

428   Alard, O., Griffin, W. L., Pearson, N. G., Lorand, J. P., and O'Reilly S. Y. (2002) New insights

429   into the Re/Os systematics of sub-continental lithospheric mantle from in-situ analysis of sulfides.

430   Earth and Planetary Science Letters, 203, 651-663.

431   Ballhaus, C., Bockrath, C., Wohlgemuth-Ueberwasser, C., Laurenz, V., and Berndt J. (2006)

432   Fractionation of the noble metals by physical processes. Contributions to Mineralogy and

433   Petrology, 152, 667–684.

434   Bockrath, C., Ballhaus, C., and Holzheid A. (2004) Fractionation of the platinum group elements

435   during mantle melting. Science, 305, 1951-1954.

436   Boehler, R. (1992) Melting of the Fe-FeO and the Fe-FeS systems at high pressure: Constraints

437   on core temperatures. Earth and Planetary Science Letters, 111, 217-227.

438   Boehler, R. (1996) Melting and element partitioning Fe-FeS temperatures to 620 kbars. Physics

439   of the Earth and Planetary Interiors, 96, 181-186.

440   Bohlen, S., and Boettcher, A. L. (1982) The quartz-coesite transformation: a precise

441   determination and the effects of other components. Journal of Geophysical Research, 87, 7073-

442   7078.

443   Bose, K., and Ganguly, J. (1995) Quartz-coesite transition revisited: reversed experimental

444   determination at 500-1200 °C and retrieved thermochemical properties, American Mineralogist,

445   80, 231-238.

446   Bulanova, G.P. (1995) The formation of diamond. Journal of Geochemical Exploration, 53, 1-23,

447   doi:10.1016/0375-6742(94)00016-5.

448   Bulanova, G. P., Griffin, W. L., Ryan, C. G., Shestakova, O. Y., and Barnes S. J. (1996) Trace

449   elements in sulfide inclusions from Yakutian diamonds, Contribution to Mineralogy and

450   Petrology, 124, 111–125.

451   Campbell, A. J., Seagleb, C. T., Heinzb, D. L., Shend, C. G., and Prakapenkae, V. B. (2007)

452   Partial melting in the iron–sulfur system at high pressure: A synchrotron X-ray diffraction study.

453   Physics of the Earth and Planetary Interiors, 162, 119–128.

21

454 Chi, H., Dasgupta, R., Duncan, M. S., Shimizu, N. (2014) Partitioning of carbon between Fe-rich

455 alloy melt and silicate melt in a magma ocean – implications for the abundance and origin of

456 volatiles in Earth, Mars, and the Moon. Geochimica et Cosmochimica Acta, 139, 447-471.

457 Dasgupta, R., M. M. Hirschmann, and C. W. Withers (2004) Deep global cycling of carbon

458 constrained by the solidus of anhydrous, carbonated eclogite under upper mantle conditions.

459 Earth and Planetary Science Letters, 227, 73-85.

460 Delpech, G., J. P. Lorand, M. Grégoirec, J. Y. Cottind, and S. Y. O'Reilly (2012) In-situ

461 geochemistry of sulfides in highly metasomatized mantle xenoliths from Kerguelen, southern

462 Indian Ocean. Lithos, 154, 296-314.

463 Eggler, D. H., Lorand, J. P. (1993) Mantle sulfide geobarometry. Geochimica et Cosmochimica

464 Acta, 57, 2213-2222.

465 Fei, Y. W., Bertka, C. M., and Finger, L. W. (1997) High-pressure iron-sulfur compound, Fe_3S_2,

466 and melting relations in the Fe-FeS system. Science, 275, 1621-1623.

467 Fram, M., and J. Longhi (1992), Phase equilibria of dikes associated with Proterozoic anorthosite

468 complexes. American Mineralogist, 77, 605-616.

469 Frost, D. J., Liebske, C., Langenhorst, F., McCammon, C. A., Trønnes, R. G., and Rubie D. C.

470 (2004) Experimental evidence for the existence of iron-rich metal in the Earth's lower mantle.

471 Nature, 428, 409-412.

472 Frost, D. J., and McCammon C. A. (2008) The redox state of Earth's mantle, Annual Review of

473 Earth and Planetary Sciences, 36, 389-420.

22

474   Gaetani, G.A., and Grove, T.L. (1997) Partitioning of moderately siderophile elements among

475   olivine, silicate melt, and sulfide melt: Constraints on core formation in the Earth and Mars.

476   Geochimica et Cosmochimica Acta, 61, 1829-1846.

477   Gaetani, G. A., and Grove T. L. (1999) Wetting of mantle olivine by sulfide melt: implications

478   for Re/Os ratios in mantle peridotite and late-stage core formation. Earth and Planetary Science

479   Letters, 169, 147-163.

480   Graham, J., Bennett, C. E. G., and Riessen A. (1987) Oxygen in pyrrhotite: 1. Thermomagnetic

481   behavior and annealing of pyrrhotites containing small quantities of oxygen. American

482   Mineralogist, 72, 599-605.

483   Graham, J., and McKenzie, C.D. (1987) Oxygen in pyrrhotite: 2. Determination of oxygen in

484   natural pyrrhotite. American Mineralogist, 72, 605-609.

485   Gunn, S. C., and Luth, R. W. (2006) Carbonate reduction by Fe-S-O melts at high pressure and

486   high temperature. American Mineralogist, 91, 1110-1116.

487   Guo, J. F., Griffin, W. L., and O'Reilly, S. Y. (1999) Geochemistry and origin of sulphide

488   minerals in mantle xenoliths: Qilin, Southeastern China. Journal of Petrology, 40, 1125–1149.

489   Hart, S. R., and Gaetani, G. A. (2006) Mantle Pb paradoxes: the sulfide solution. Contributions

490   to Mineralogy and Petrology, 152, 295-308.

491   Helffrich, G., Kendall, M., Hammond, J. O. S., and Carroll, M. R. (2011) Sulfide melts and long-

492   term low seismic wavespeeds in lithospheric and asthenospheric mantle. Journal of Geophysical

493   Research, 38, 11301-11305, doi:10.1029/2011GL047126.

23

494   Hirschmann, M. M. (2000) Mantle solidus: Experimental constraints and the effects of peridotite

495   composition. Geochemistry, Geophyics, Geosystems., 1, 2000GC000070.

496   Hsieh, K. C., Schmid, R., and Chang, Y. A. (1987) The Fe-Ni-S system II. A Thermodynamic

497   model for the ternary monosulfide phase with the nickel arsenide structure. High Temperature

498   Science, 23, 39-52.

499   Huang, S., Lee, C. T., and Yin, Q. Z. (2014) Missing lead and high ^{3}He/^{4}He in ancient sulfides

500   associated with continental crust formation. Nature Scientific Reports, 4, 5314,

501   doi:10.1038/srep05314.

502   Jones, J. H., and Walker, D. (1991) Partitioning of siderophile elements in the Fe-Ni-S system: 1

503   bar to 80 kbar. Earth and Planetary Science Letters, 105, 127-133.

504   Katsura, T., Yoneda, A., Yamazaki, D., Yoshino, T., and Ito, E. (2010) Adiabatic temperature

505   profile in the mantle. Physics of Earth and Planetary Interiors, 183, 212-218.

506   Katz, R. F., Spiegelman, M., and Langmuir, C. H. (2003) A new parameterization of hydrous

507   mantle melting. Geochemistry, Geophyics, Geosystems., 4 (9), 1073.

508   Kullerud, G. (1963) Thermal stability of pentlandite. Canadian Mineralogist, 7, 353-366.

509   Li, Y. and Audétat, A. (2012) Partitioning of V, Mn, Co, Ni, Cu, Zn, As, Mo, Ag, Sn, Sb, W, Au,

510   Pb, and Bi between sulfide phases and hydrous basanite melt at upper mantle conditions.

511   Lorand, J. P. (1989) Abundance and distribution of Cu-Fe-Ni sulfides, sulfur, copper and

512   platinum-group elements in orogenic-type spinel lherzolite massifs of Arirge (northeastern

513   Pyrenees, France). Earth and Planetary Science Letters, 93, 50-64.

514   Lorand, J. P., and Alard, O. (2001) Platinum-group element abundances in the upper mantle:

515   New constraints from in situ and whole-rock analyses of Massif Central xenoliths (France).

516   Geochimica et Cosmochimica Acta, 65, 2789–2806.

517   Lorand, J. P., Delpech, Guillaume., Gre´goire, M., Moine, B., O'Reilly, S. Y., and Cottin, J-Y.

518   (2004)   Platinum-group elements and the multistage metasomatic history of Kerguelen

519   lithospheric mantle (South Indian Ocean). Chemical Geology, 208, 195–215.

520   Lorand, J. P., Luguet, A., and Alard, O. (2013) Platinum-group element systematics and

521   petrogenetic processing of the continental upper mantle: A review. Lithos, 164–167, 2–21.

522   Luo, S. N., Mosenfelder, J. L., Asimow, P.D., and Ahrens, T. J. (2002) Direct shock wave

523   loading of Stishovite to 235 GPa: Implications for perovskite stability relative to an oxide

524   assemblage   at   lower   mantle   conditions.   Journal   of   Geophysical   Research,   29,

525   doi:10.1029/2002GL015627.

526   McDade, P., Wood, B.J., Van Westrenen, W., Brooker, R., Gudmundsson, G., Soulard, H.,

527   Najorka, J., and Blundy, J. (2002) Pressure corrections for a selection of piston-cylinder cell

528   assemblies. Mineralogical Magazine, 66, 1021-1028.

529   McDonough, W. F., and Sun, S. S. (1995) The composition of the Earth. Chemical Geology, 120,

530   223-253.

531   Mirwald, P. W., Getting, I. C., and Kennedym, G. C. (1975) Low-friction cell for piston-cylinder

532   high-pressure apparatus. Journal of Geophysical Research, 80, 1519-1525.

25

533   Mirwald, P. W., and Kennedy, G. C. (1979) The melting curve of gold, silver, and copper to 60

534   Kbar pressure: a reinvestigation. Journal of Geophysical Research, 84, 6750-6756.

535   Morard, G., Andrault, D., Guignot, N., Siebert, J., Garbarino, G., and Antonangeli, D. (2011)

536   Melting of Fe–Ni–Si and Fe–Ni–S alloys at megabar pressures: implications for the core–mantle

537   boundary temperature. Physics and Chemistry of Minerals, 38, 767-776.

538   Mungall, J. E., and Su, S. G. (2005) Interfacial tension between magmatic sulfide and silicate

539   liquids: Constraints on kinetics of sulfide liquation and sulfide migration through silicate rocks.

540   Earth and Planetary Science Letters, 234, 135-149.

541   Pearson, D. G., Shirey, S. B., Harris, J. W., and Carlson, R. W. (1998) Sulphide inclusions in

542   diamonds from the Koffiefontein kimberlite, S Africa: constraints on diamond ages and mantle

543   Re–Os systematics. Earth and Planetary Science Letters, 160, 311-326.

544   Pearson, D. G., Canil, D., and Shirey, S. B. (2003) Mantle samples included in volcanic rocks:

545   xenoliths and diamonds. Treatise on Geochemistry, 2, 171-275.

546   Pearson, D. G., Parman, S. W. and Nowell, G. M. (2007) A link between large mantle melting

547   events and continent growth seen in osmium isotopes. Nature, 449, 202-205.

548   Pearson, D.G., and Wittig, N. (2014) The formation and evolution of cratonic mantle lithosphere:

549   Evidence from mantle xenoliths, in Treatise on Geochemistry, 2nd ed., edited by H. D. Holland

550   and K. K. Turekian, pp. 255–292, Elsevier, Oxford.

551   Pearson, N. J., Alard, O., Griffin, W. L., Jackson, S. E., and O'Reilly, S. Y. (2002) In situ

552   measurement of Re-Os isotopes in mantle sulfides by laser ablation multicollector-inductively

553 coupled plasma mass spectrometry: analytical methods and preliminary results. Geochimica et

554 Cosmochimica Acta, 66, 1037-1050.

555 Pollack, H. N., and Chapman, D. S. (1977) On the regional variation of heat flow, geotherms,

556 and lithospheric thickness. Tectonophysics, 38, 279-296.

557 Powell, W., and O'Reilly, S. Y. (2007) Metasomatism and sulfide mobility in lithospheric

558 mantle beneath eastern Australia: Implications for mantle Re–Os chronology. Lithos, 94, 132-

559 147.

560 Richardson, S. H., Shirey, S. B., Harris, J. W., and Carlson, R. W. (2001) Archean subduction

561 recorded by Re-Os isotopes in eclogitic sulfide inclusions in Kimberley diamonds. Earth and

562 Planetary Science Letters, 191, 257-266.

563 Rohrbach, A., Ballhaus, C., Gola-Schindler, U., Ulmer, P., Kamnetsky, V.S., and Kuzmin, D.V.

564 (2007) Metal saturation in the upper mantle. Nature, 449, 456-460.

565 Rohrbach, A., Ballhaus, C., Ulmer, P., Kamnetsky, V.S., and Gola-Schindler, U. (2011)

566 Experimental evidence for a reduced metal-saturated upper mantle. Journal of Petrology, 52,

567 717-731.

568 Roy-Barman, M., Wasserburga, G.J., Papanastassioua, D.A., and Chaussidon, M. (1998)

569 Osmium isotopic compositions and Re–Os concentrations in sulfide globules from basaltic

570 glasses. Earth and Planetary Science Letters, 154, 331 -347.

571 Ryzhenko, B., and Kennedy, G. C. (1973) The effect of pressure on the eutectic in the system

572 Fe-FeS. American Journal of Science, 273, 803-810.

27

573   Shannon, M. C., and Agee, C. B. (1998) Percolation of core melts at Lower Mantle Conditions.

574   Science, 280, 1059-1061.

575   Sharp, W. E. (1969) Melting curves of sphalerite, galena, and pyrrhotite and the decomposition

576   curve of pyrite between 30 and 65 kilobars. Journal of Geophysical Research, 74, 1645-1652.

577   Shi, C. Y., Zhang, L., Yang., W, Liu, Y., Wang, J., Meng, Y., Andrews, J. C., and Mao, W.L.

578   (2013) Formation of an interconnected network of iron melt at Earth's lower mantle conditions.

579   Nature Geoscience, 6, 971–975.

580   Shirey, S. B., and Richardson, S. H. (2011) Start of the Wilson cycle at 3 Ga shown by diamonds

581   from subcontinental mantle. Science, 333, 434-436.

582   Shirey S. B., Cartigny, P., Frost, D. J., Keshav, S., Paolo Nimis, F. N., Pearson, D. G., Sobolev,

583   N. V., and Walter, M. J. (2013) Diamonds and the geology of mantle carbon. Reviews in

584   Mineralogy and Geochemistry, 75, 355-421.

585   Simons, F., and Glatzel, G. (1929) Bemerkungen zur Schmelzdruckkurve. Zeitschrift für

586   anorganische und allgemeine Chemie, 178, 309-316.

587   Stewart, A. J., Schmidt, M. W., Westrenen, W. V., and Liebske, C. (2007) Mars: A new core-

588   crystallization regime. Science, 316, 1323-1325.

589   Stachel, T., and Harris, J.W. (2008) The origin of cratonic diamonds – constraints from mineral

590   inclusions. Ore Geology Reviews, 34, 5-32.

28

591   Tenner, T. J., Hirschmann, M. M., Withers, C. W., and Hervig, R. L. (2012) H_2O storage

592   capacity of olivine and low-Ca pyroxene from 10 to 13 GPa: consequences for dehydration

593   melting above the transition zone. Contribution to Mineralogy and Petrology, 163, 297-316.

594   Turcotte, D. L., and Schubert, G. (2002) Geodynamics, 2nd ed., pp. 456, Cambridge University

595   Press, Cambridge.

596   Urakawa, S., Kato, M., and Kumazawa, M. (1987) Experimental study on the phase relations in

597   the system Fe-Ni-O-S up to 15 GPa, in High-Pressure Research in Mineral Physics, edited by M.

598   H. Manghnani and Y. Syono, pp. 95–111, Terrapub, Tokyo.

599   Usselman, T. (1975) Experimental approach to the state of the core: Part I. The liquidus relations

600   of the Fe-rich portion of the Fe-Ni-S system from 30 to 100 kbars. American Journal of Science,

601   275, 278-290.

602   Waldner, P., and Pelton A. (2004) Critical thermodynamic assessment and modeling of the Fe-

603   Ni-S system. Metallurgical and Materials Transactions B, 35, 897-907.

604   Westerlund, K. J., Shirey, S. B., Richardson, S. H., Carlson, R. W., Gurney, J. J., and Harris, J.

605   W. (2006) A subduction wedge origin from Paleoarchaean peridotitic diamonds and harzburgites

606   from the Panda kimberlite, Slave craton: evidence from Re-Os isotope systematics.

607   Contributions to Mineralogy and Petrology, 152, 275-294.

608   Withers, A. C., and Hirschmann, M. M. (2007) H_2O storage capacity of $MgSiO_3$ clinoenstatite at

609   8–13 GPa, 1,100–1,400 °C. Contributions to Mineralogy and Petrology, 154, 663-674.

610   Xirouchakis, D., Hirschmann, M. M., and Simpson, J. A. (2001) The effect of titanium on the

611   silica content and on mineral–liquid partitioning of mantle-equilibrated melts. Geochimica et

612   Cosmochimica Acta, 65, 2201–2217.

613

FIGURE CAPTIONS

614

FIGURE 1. Melting relations from selected previous sulfide melting experiments up to 15 GPa.

615

616   Compositions and data sources are given in Table 1.

617   **FIGURE 2.** (a) Sulfide compositions projected into the metal-sulfur-oxygen atomic ternary.

618   Metal is the sum of Fe, Ni and Cu. Natural sulfide compositions are taken from bulk composition

619   estimates of sulfides trapped in diamonds and olivine as inclusions (Aulbach et al. 2009;

620   Bulanova et al. 1996; Westerlund et al. 2006;); (b) Sulfide compositions projected into the Fe-S-

621   Ni ternary. Minor amounts of Cu and O have been projected to the Ni and S apices, respectively.

622   The yellow and pink areas correspond to the fields of stability of mss and mss+melt at 0.1 MPa,

623   1000 °C (Hsieh et al. 1987). Numbered circles refer to sulfide compositions that have been

624   investigated experimentally, as listed in Table 1. Natural sulfide compositions are plotted as grey

625   circles from the same references as (a).

626   **FIGURE 3.** Optical images of Au recovered from pressure and temperature calibration

627   experiments. Gold spheroids are produced from experiments that exceeded the melting

628   temperature of Au, whereas relict wires are observed from experiments that remained below the

629   Au fusion curve.

30

630   **FIGURE 4.** Revised pressure and temperature calibrations of multi-anvil device at UMN using

631   the 18/12 TEL/OEL assembly. (a) Pressure-force relations of the best fit functions are $P = -1.15$

632   x $10^{-5} F^2 + 2.44$ x $10^{-2} F + 4.56$ x 10^{-3} for 1000-1200 °C (Dasgupta et al. 2004), $P = -1.29$ x 10^{-5}

633   $F^2 + 2.61$ x $10^{-2} F - 5.17$ x 10^{-3} for 1200-1400 °C (this study), and $P = -1.65$ x $10^{-5} F^2 + 3.03\ 10^{-2}$

634   $F - 1.76$ x 10^{-3} for 1400-1700 °C (unpublished data), where P is pressure (GPa) and F is force

635   (tons). The blue square corresponds to 170 tons and 3.49-3.53 GPa (Tenner et al. 2009) and the

636   purple circles represent coesite and red diamonds represent quartz; (b) Temperature calibration

637   results on PC and MA. Thermocouple temperatures and corrected sample pressures are plotted

638   together with gold melting curve calibrated with previous calibration work by Mirwald and

639   Kennedy (1979). Lower temperatures read by thermocouples compared to the fusion curve

640   reflect the offset in temperature between the thermocouple location and the sample hotspot.

641   **FIGURE 5.** Backscattered electron images of typical textures from quenched experiments

642   exemplifying (a) super-liquidus conditions (B536: 1.8 GPa, 1300 °C), (b) partially molten

643   (A1075: 1.8 GPa, 1200 °C), and (c) subsolidus (B534: 1.8 Ga, 1100 °C).

644   **FIGURE 6.** Experimentally determined melting relations of $Fe_{0.69}Ni_{0.23}Cu_{0.02}S_{1.00}$. Blue

645   diamonds are sub-solidus mss, with filled diamonds from piston cylinder (PC) experiments and

646   empty diamonds from those conducted in the multi-anvil (MA), respectively. Red and orange

647   circles are melt-mss pairs by PC and MA, respectively. Green and black triangles are

648   superliquidus runs by PC and MA, respectively. Solid curve is the parameterization of the

649   solidus, given by $T(°C) = 1015.1[P(GPa)/1.88+1]^{0.206}$ and the dashed curve is liquidus, given by

650   $T(°C) = 1067.3[P(GPa)/1.19+1]^{0.149}$. Melting relations at 0.1 MPa are taken from Bockrath et al.

651   (2004).

31

652 **FIGURE 7.** Comparison of mss melting relations calibrated from experiments in this study (Fig.

653 6) with experiments done by Bockrath et al. (2004). Diamonds are sub-solidus mss; circles are

654 melt-mss pairs; triangles are superliquidus runs. The square bracket with a red filling and green

655 triangle is the "problem bracket", which is labeled as "melt + solid" by Bockrath et al. (2004),

656 but is listed as "solid only" in their supplementary material. Our results suggest that the

657 experiment should have been completely melted at the stated run conditions. The solidus and

658 liquidus derived from the parameterization of the present study (Fig. 6) are shown as solid and

659 dashed curves, respectively.

660 **FIGURE 8.** Comparison of melt fractions calculated by Fe and Ni mass balance. Calculations

661 are in close agreement, but those from Ni are believed to be more accurate because

662 concentrations of Ni are more distinct in mss and partial melts, giving more leverage to

663 calculated mass balances.

664 **FIGURE 9.** Variations in mss/melt partition coefficient of Cu, Ni and Fe as a function of Ni

665 content of the melt. Partitioning of Cu and Ni between crystalline and solid sulfide is more

666 extreme for Ni-rich smaller-degree partial melts, and less so for higher-degree Fe-rich melts.

667 **FIGURE 10.** Comparison of mss solidus (solid black curve) and liquidus (dashed black curve)

668 with mantle geotherms and domains of potential silicate melting. The mantle adiabat is given in

669 the solid red line, with the shaded area representing the temperature uncertainty (Katsura et al.

670 2010). A geotherm applicable to oceanic lithosphere of plate ages ranging from 20 Ma and 80

671 Ma is calculated from a cooling half-space model (Turcotte and Schubert 2002) and

672 representative continental geotherms are shown in the shaded dark areas, bounded by

673 calculations for heat flows of 40 mW/m^2 and 50 mW/m^2 (Pollack and Chapman 1977). Regions

32

674   of diamond formation as inferred from inclusion thermobarometry are from Stachel and Harris

675   (2008) in green loop and Shirey et al (2013) in pink loop. The solidus of nominally anhydrous

676   peridotite is shown as the green solid curve (Hirschmann 2000); hydrous peridotite (0.1 wt.%

677   bulk water) is the blue solid curve (Katz et al. 2003).

Figure. 1
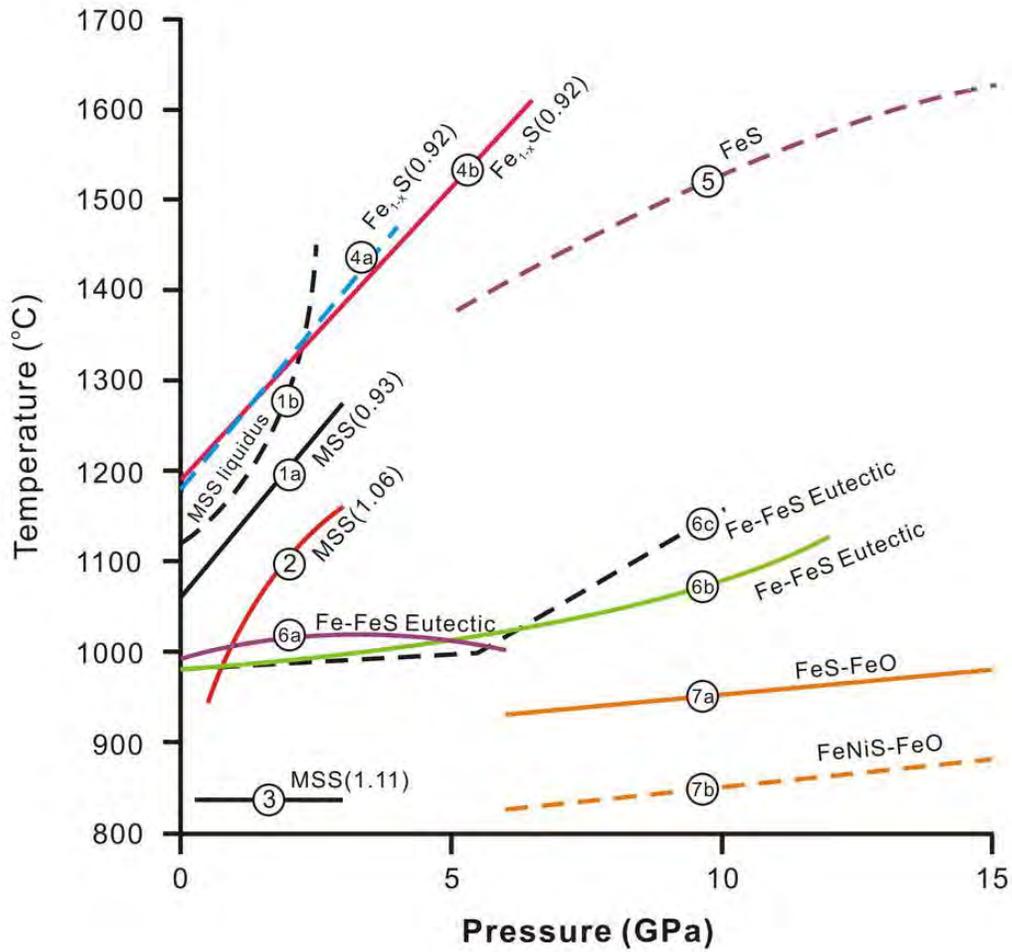
Figure. 2
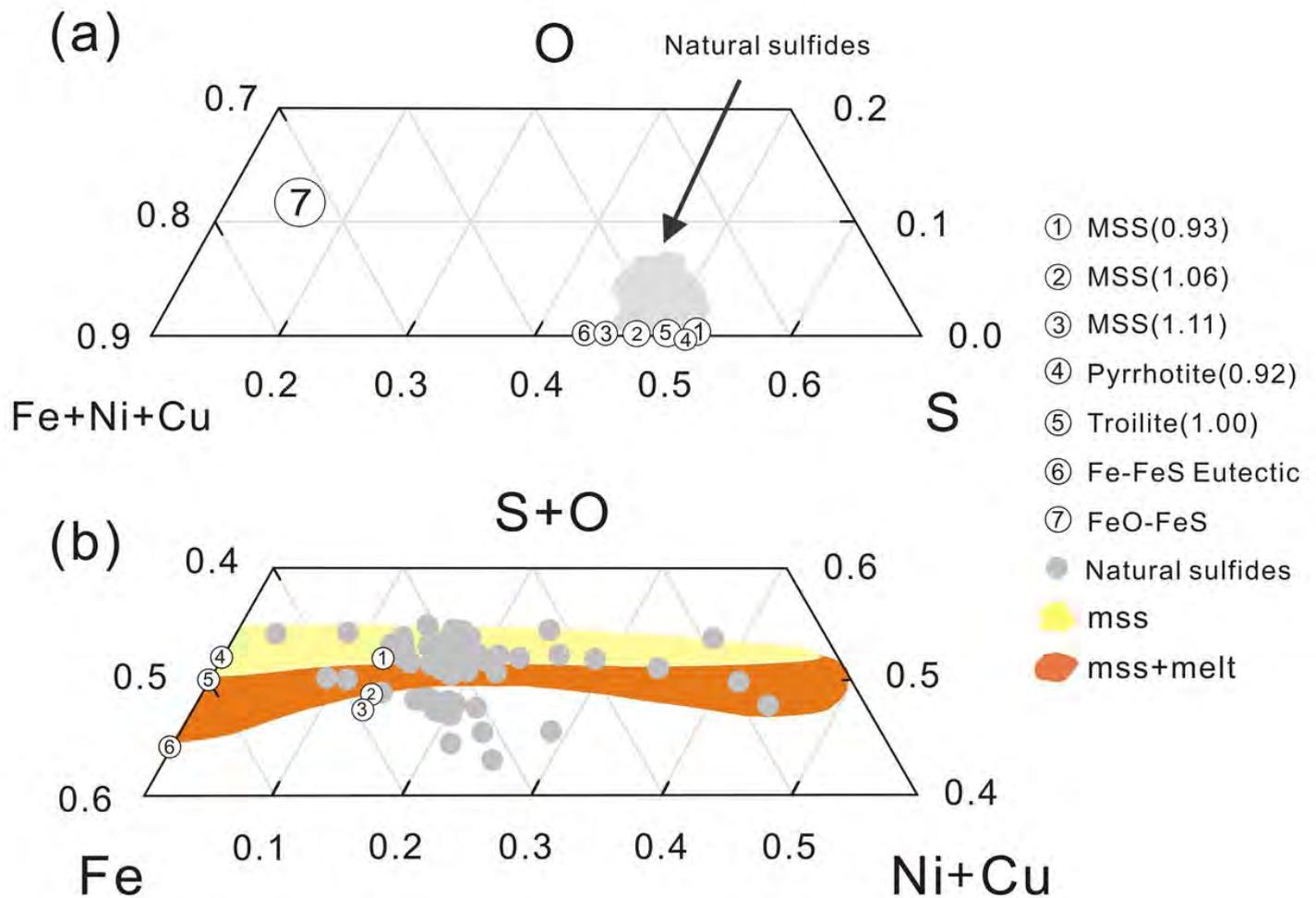
Figure. 4
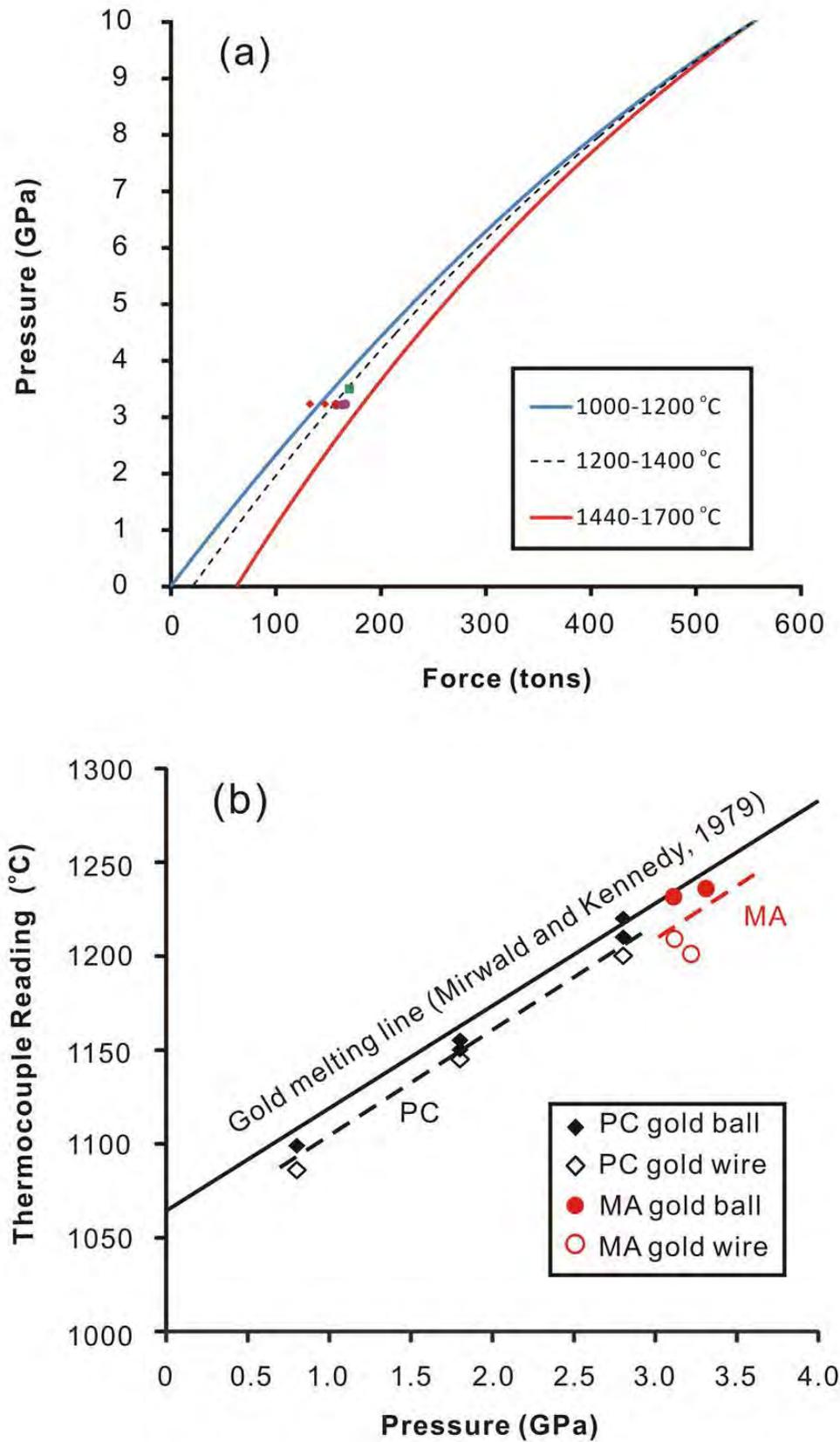
Figure. 5
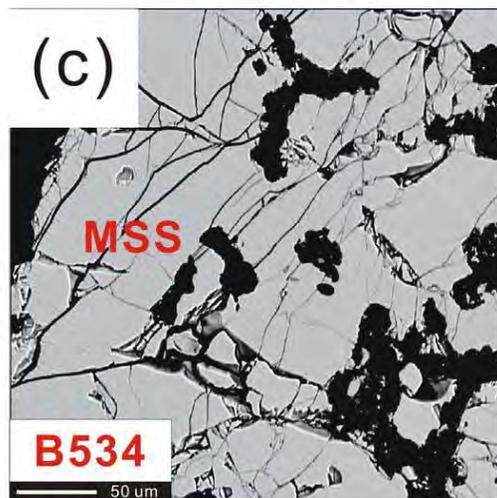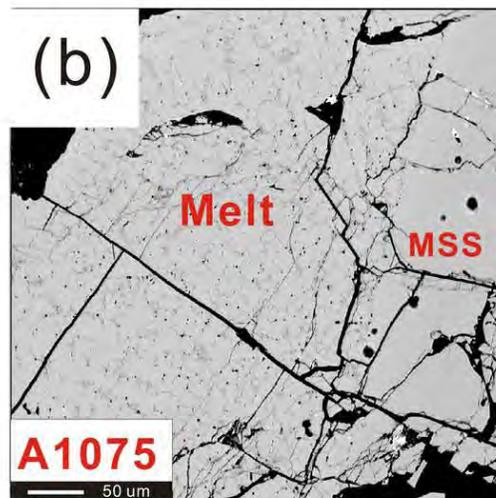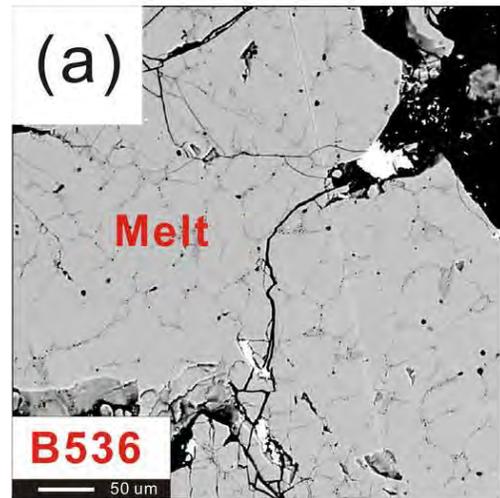
Figure. 3
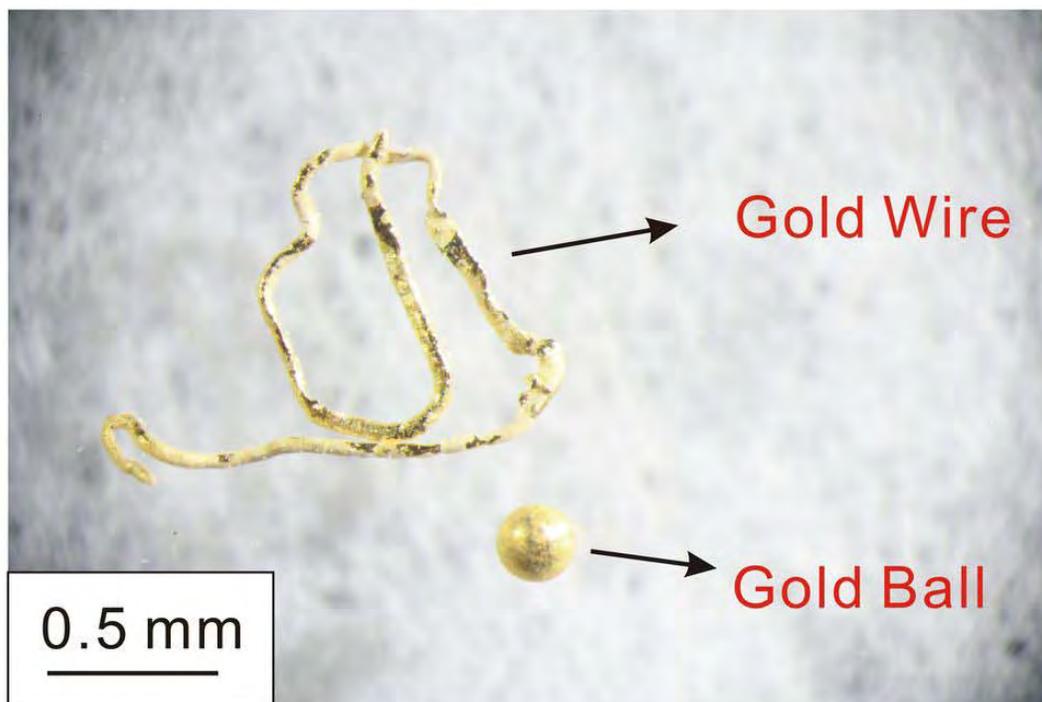
Figure. 6
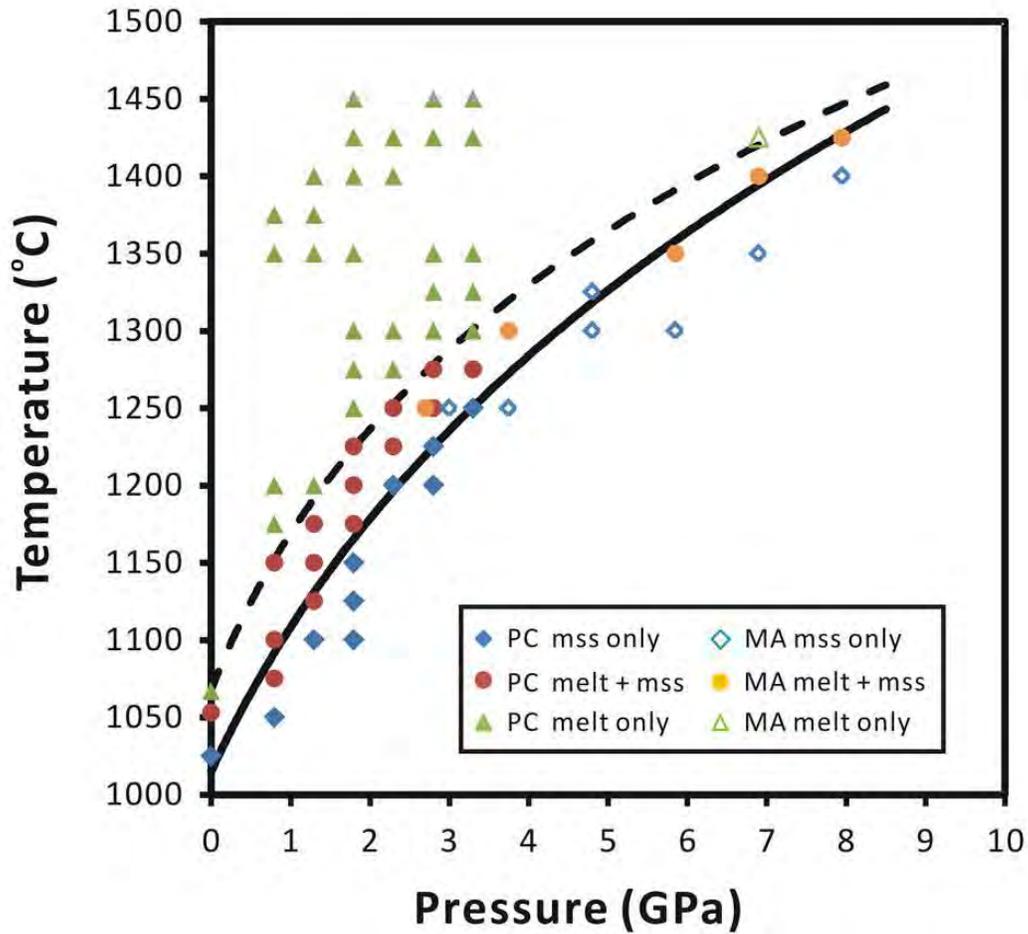
Figure. 7
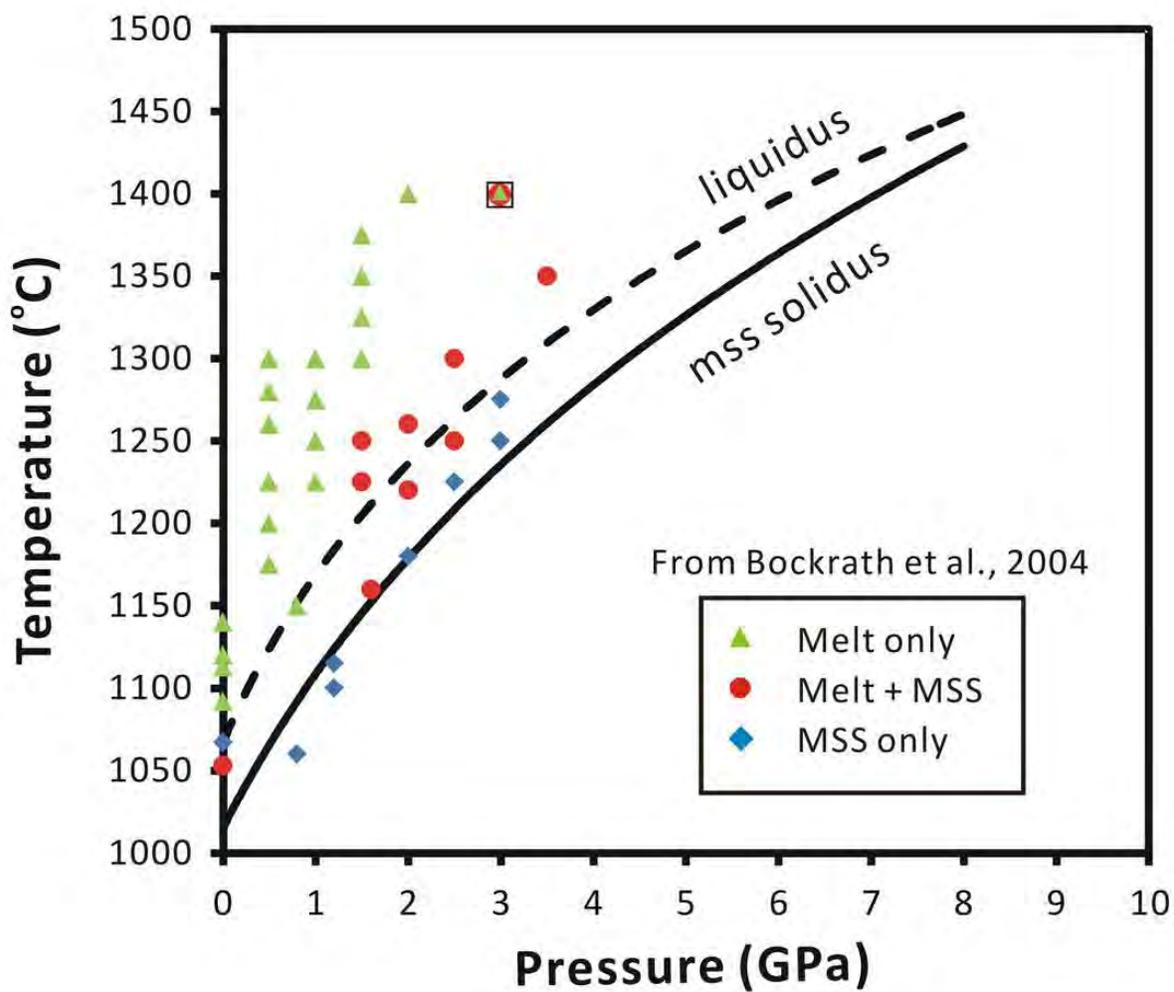
Figure. 8
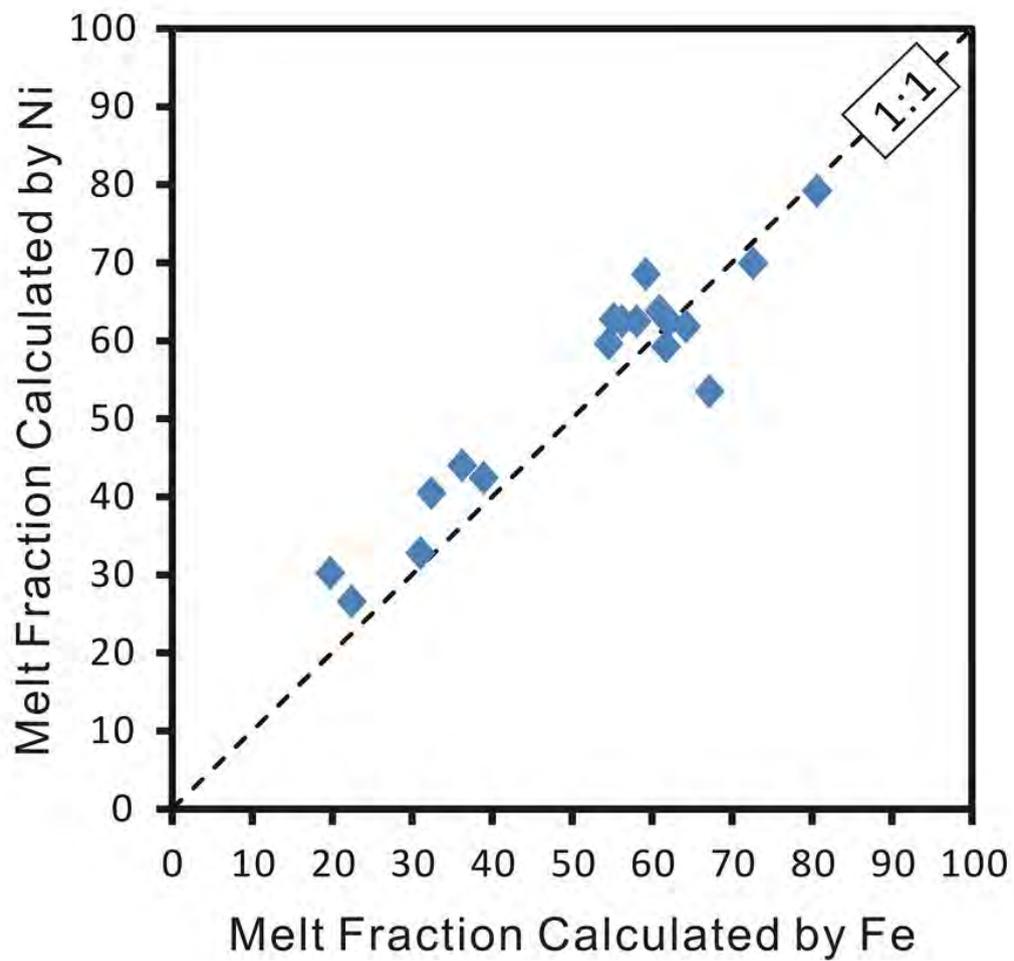
Figure. 9
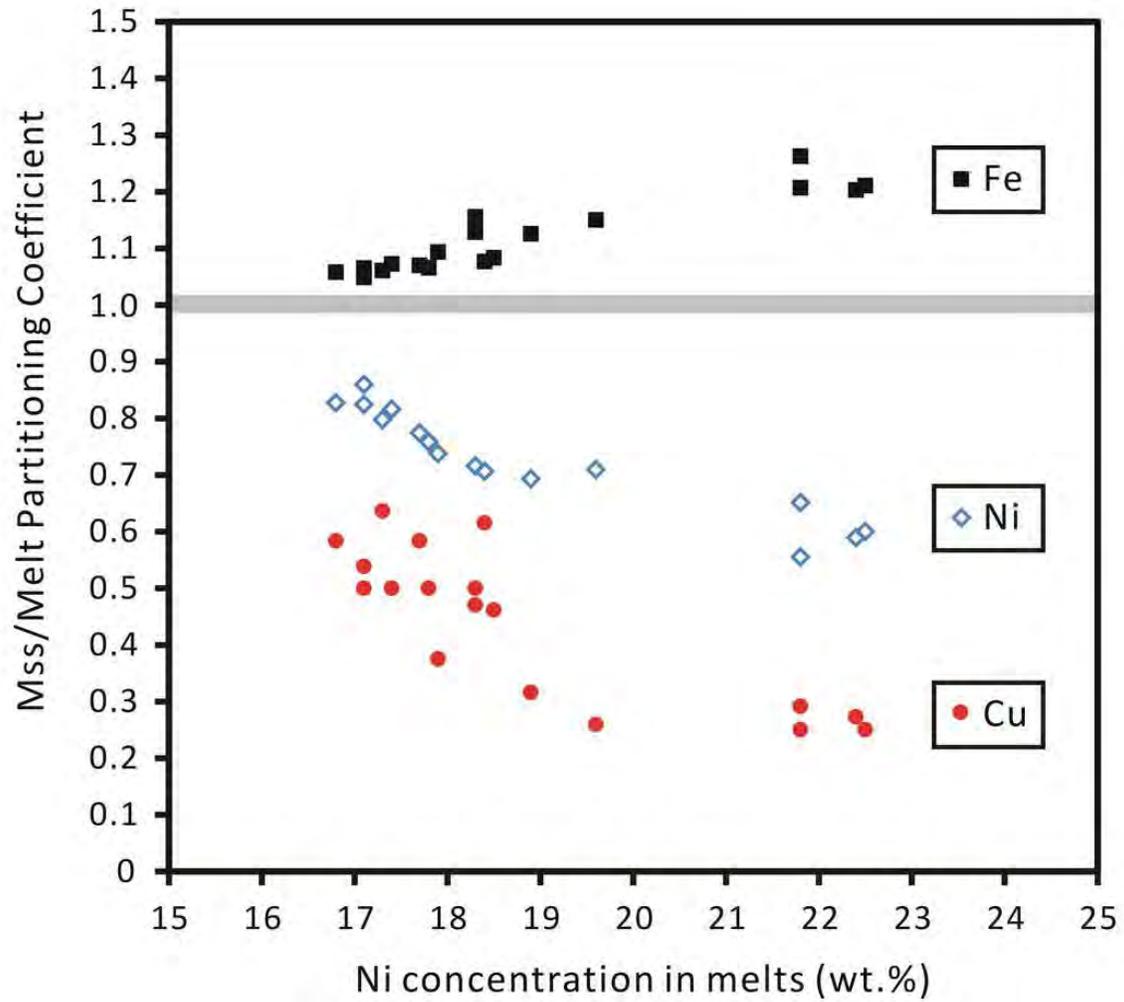
Figure. 10
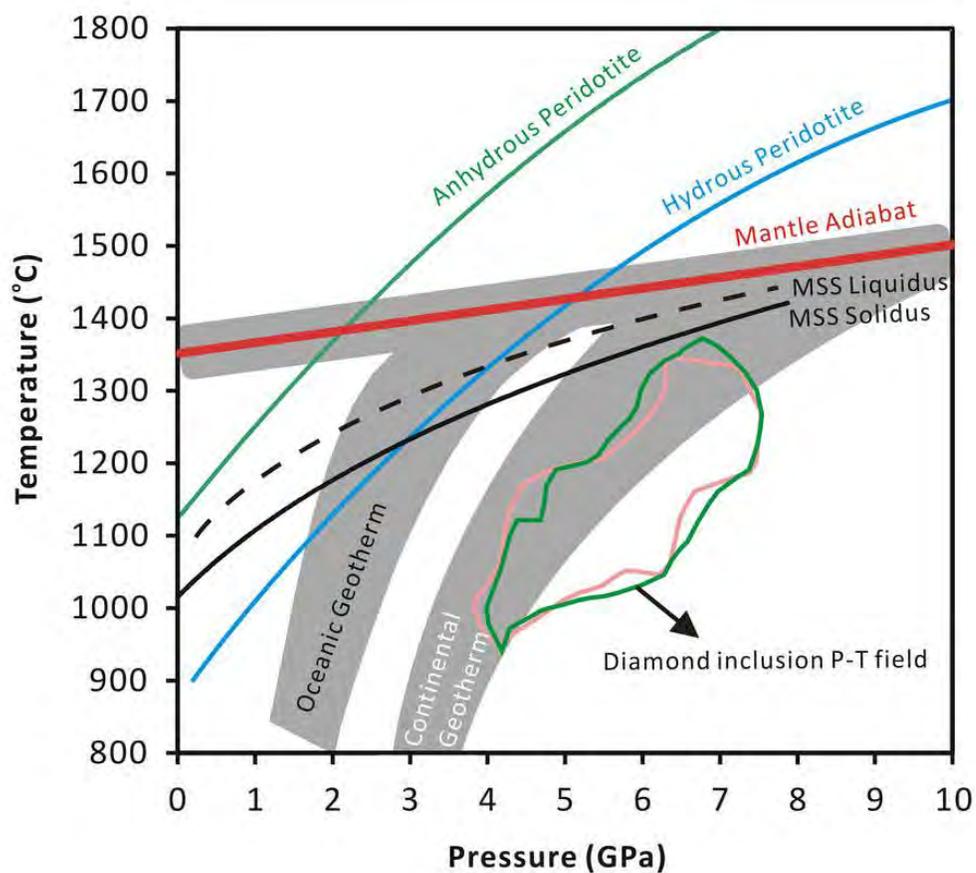
TABLE 1. Summary of high pressures studies on sulfide melting up to 15 GPa

#	Description*	Chemical Formula (atomic)		Chemical Composition (wt.%)					Capsule	Apparatus‡	References
				Fe	Ni	Cu	O	S			
	MSS (0.93)	$Fe_{0.69}Ni_{0.23}Cu_{0.01}$	$S_{1.00}$	45.3	15.8	1.0	--	37.9	silica glass	PC + MA	This study
1a	MSS (0.93) solidus	$Fe_{0.69}Ni_{0.23}Cu_{0.01}$	$S_{1.00}$	45.3	15.8	1.0	--	37.9	silica glass	PC	Bockrath et.al, 2004
1b	MSS (0.93) liquidus	$Fe_{0.69}Ni_{0.23}Cu_{0.01}$	$S_{1.00}$	45.3	15.8	1.0	--	37.9	silica glass	PC	Bockrath et.al, 2004
2	MSS (1.06) solidus	$Fe_{0.79}Ni_{0.25}Cu_{0.03}$	$S_{1.00}$	47.9	15.6	1.9	--	34.7	silica glass	PC	Ballhaus et.al, 2006
3	MSS (1.11) solidus	$Fe_{0.83}Ni_{0.25}Cu_{0.03}$	$S_{1.00}$	48.9	15.5	1.9	--	33.7	silica glass	PC	Ballhaus et.al, 2006
4a	Pyrrhotite (0.92)	$Fe_{0.92}$	$S_{1.00}$	62.0	--	--	--	38.0	alumina	PC	Ryzhenko and Kennedy, 1979
4b	Pyrrhotite (0.92)	$Fe_{0.92}$	$S_{1.00}$	62.0	--	--	--	38.0	soda glass	BA	Sharp, 1969
5	Troilite	$Fe_{1.00}$	$S_{1.00}$	63.5	--	--	--	36.5	--	DAC	Boehler, 1992
6a	Fe-FeS Eutectic†	$Fe_{1.18}$	$S_{1.00}$	69.0	--	--	--	31.0	alumina	PC	Ryzhenko and Kennedy, 1979
6b	Fe-FeS Eutectic†	$Fe_{1.18}$	$S_{1.00}$	69.0	--	--	--	31.0	--	DAC	Boehler, 1996
6c	Fe-FeS Eutectic†	$Fe_{1.18}$	$S_{1.00}$	69.0	--	--	--	31.0	boron nitride	BA	Usselman, 1975
7a	FeS-FeO	$Fe_{5.28}O_{1.08}$	$S_{1.00}$	85.7	--	--	5.0	9.3	MgO	MA	Urakawa, 1987
7b	(Fe,Ni)S-FeO	$Fe_{4.41}Ni_{0.49}O_{0.50}$	$S_{1.00}$	78.2	9.1	--	2.5	10.2	MgO	MA	Urakawa, 1987

Notes: # refers to the curves labeled in Fig. 2. * Number in parentheses represents metal/sulfur atomic ratio. † The eutectic composition at 1 atmosphere. ‡ PC: piston cylinder; MA: multianvil; DAC: diamond anvil cell; BA: belt apparatus

TABLE 2. Pressure and temperature calibration experiments using the quartz-coesite transition and gold fusion

Quartz - coesite transition experiments

PC Run #	Uncorrected Pressure (GPa)	T (°C)	t (hrs)	Run product
A1199	3.50	1100	6	coesite
A1204	3.70	1100	6	coesite
A1209	3.30	1100	6	quartz
A1210	3.10	1100	6	quartz
A1218	3.45	1100	6	quartz
A1219	3.40	1100	6	quartz

MA Run #	Force (metric tons)	T (°C)	t (hrs)	Run product
M767	165	1250	2	coesite
M770	160	1220	2	coesite
M771	155	1230	2	coesite
M749	145	1250	3	quartz
M743	131	1250	3	quartz
M762	155	1250	2	quartz

Gold melting experiments

PC Run #	Corrected Pressure (GPa)	Tc reading (°C)	t (hrs)	Run product
A1141	0.80	1086	0.1	gold wire
A1137	1.80	1145	0.1	gold wire
A1144	2.80	1200	0.1	gold wire
A1135	1.80	1155	0.1	gold ball
A1142	1.80	1150	0.1	gold ball
A1139	0.80	1099	0.1	gold ball
A1156	2.80	1220	0.1	gold ball
A1147	2.80	1210	0.1	gold ball

MA Run #	Corrected Pressure (GPa)	Tc reading (°C)	t (hrs)	Run product
M762	3.23	1230	0.1	gold ball
M767	3.43	1232	0.1	gold ball
M770	3.33	1200	0.1	gold wire
M771	3.23	1210	0.1	gold wire

TABLE 3. Experimental results and sulfide compositions by electron microprobe analysis.

	P (GPa)	T (°C)	t (hrs)	n^a	Results	Cu	O	S	Fe	Ni	Total	M/S^b	F_{Fe}^c	F_{Ni}^c
								Chemical Composition (wt.%)						
Subsolidus runs: solid only														
A1078	0.8	1050	15	22	mss	0.9	0.4	37.3	45.8	15.7	100.1	0.93	-	-
A1080	1.3	1100	13	24	mss	1.1	0.5	37.1	45.6	16.1	100.4	0.93	-	-
B107	1.8	1100	24	12	mss	0.9	0.4	37.4	45.5	16.1	100.2	0.92	-	-
A1081	1.8	1125	20	18	mss	1.1	0.5	36.6	45.7	16.1	99.9	0.95	-	-
A1076	1.8	1150	14	19	mss	0.9	0.3	36.6	46.1	16.3	100.2	0.96	-	-
B554	2.3	1200	18	18	mss	1.1	0.3	37.2	45.0	16.2	99.8	0.94	-	-
B641	2.8	1200	12	12	mss	1.0	0.4	36.4	45.5	16.4	99.6	0.96	-	-
A1231	2.8	1225	12	20	mss	0.9	0.4	36.7	45.5	16.2	99.7	0.94	-	-
M749	3.0	1250	4	14	mss	0.9	0.3	37.1	45.6	15.8	99.7	0.94	-	-
B556	3.3	1250	18	14	mss	1.0	0.3	36.9	45.6	16.6	100.5	0.95	-	-
M721	3.75	1250	8	10	mss	1.0	0.4	37.6	45.2	16.1	100.3	0.92	-	-
M742	4.8	1300	4	25	mss	1.0	0.3	36.5	45.6	16.4	99.8	0.96	-	-
M734	5.85	1300	8	16	mss	1.1	0.3	37.3	45.2	16.2	100.0	0.93	-	-
M744	6.9	1350	1	36	mss	1.1	0.3	36.4	45.1	16.7	99.7	0.96	-	-
M746	7.95	1400	1	8	mss	1.0	0.3	36.9	45.7	16.5	100.4	0.95	-	-
Between solidus and liquidus: melt-mss pairs														
A1079	0.8	1075	14	14	melt	2.2	0.3	36.1	39.9	22.4	100.9	0.99	31	33
				18	mss	0.6	0.3	38.1	48.0	13.2	100.1	0.91		
A1077	0.8	1100	14	12	melt	1.7	0.3	36.4	42.5	18.3	99.3	0.95	55	60
				8	mss	0.8	0.2	37.9	49.1	13.1	101.1	0.93		
B633	0.8	1150	8	26	melt	1.2	0.5	36.1	44.4	17.1	99.3	0.95	62	62
				15	mss	0.6	0.3	37.8	47.3	14.7	100.8	0.92		
A1087	1.3	1125	17	25	melt	2.7	0.3	36.6	41.3	19.6	100.4	0.96	32	40
				31	mss	0.7	0.4	37.9	47.5	13.9	100.3	0.91		
B617	1.3	1150	6	22	melt	1.2	0.3	36.5	44.2	17.7	99.9	0.96	58	63
				14	mss	0.7	0.3	37.4	47.3	13.7	99.5	0.92		
B618	1.3	1175	12	17	melt	1.3	0.4	37.1	44.9	17.1	100.8	0.94	73	70
				10	mss	0.7	0.3	38.1	47.1	14.1	100.2	0.91		
A1128	1.8	1175	6	15	melt	1.9	0.3	34.9	43.7	18.9	99.8	1.02	67	53
				14	mss	0.6	0.2	37.9	49.2	13.1	100.9	0.93		
A1075	1.8	1200	16	16	melt	1.6	0.2	35.8	43.9	17.9	99.4	0.99	61	64
				16	mss	0.6	0.3	38.1	48.0	13.2	100.1	0.91		

	P (GPa)	T (°C)	t (hrs)	n[a]	Results	Cu	O	S	Fe	Ni	Total	M/S[b]	F_{Fe}[c]	F_{Ni}[c]
						Chemical Composition (wt.%)								
B607	1.8	1225	6	18	melt	1.2	0.3	36.4	45.0	16.8	99.7	0.96	81	79
				20	mss	0.7	0.5	37.7	47.6	13.9	100.4	0.91		
A1114	2.30	1225	18	12	melt	2.4	0.3	35.8	39.2	21.8	99.5	0.98	39	42
				10	mss	0.7	0.2	37.6	49.5	12.1	100.1	0.92		
A1177	2.3	1250	12	17	melt	1.4	0.3	36.6	44.1	17.4	99.8	0.95	56	63
				14	mss	0.7	0.3	37.8	47.3	14.2	100.3	0.92		
M743	2.7	1250	3	24	melt	2.4	0.4	36.0	38.9	22.5	100.2	0.97	20	30
				16	mss	0.6	0.3	37.5	47.1	13.5	99.1	0.91		
B556	2.8	1250	18	24	melt	2.4	0.3	35.8	39.2	21.8	99.5	0.98	22	26
				31	mss	0.6	0.3	37.7	47.3	14.2	100.1	0.92		
B564	2.8	1275	12	16	melt	1.1	0.3	37.0	44.4	17.3	100.2	0.95	59	69
				12	mss	0.7	0.4	38.1	47.1	13.8	100.0	0.90		
A1157	3.3	1275	0.5	24	melt	1.2	0.4	36.0	44.2	17.8	99.7	0.97	55	63
				33	mss	0.6	0.3	37.5	47.1	13.5	99.1	0.91		
M716	3.75	1300	8	12	melt	1.3	0.2	36.2	44.2	18.4	100.3	0.99	62	59
				12	mss	0.8	0.2	37.8	47.6	13.0	99.4	0.91		
M724	5.85	1350	8	24	melt	1.6	0.3	36.4	43.5	18.3	100.2	0.97	64	62
				8	mss	0.8	0.2	37.9	49.1	12.8	100.8	0.93		
M794	6.9	1400	1	12	melt	1.1	0.3	36.6	43.6	17.8	99.5	0.95		
M798	7.95	1425	1	10	melt	1.3	0.5	36.1	43.2	18.5	99.7	0.96	36	44
				12	mss	0.6	0.2	37.6	46.8	14.4	99.6	0.92		
Superliquidus runs: melt only														
B636	0.8	1175	8	18	melt	1.0	0.4	36.4	45.2	16.4	99.3	0.95	-	-
B600	0.8	1375	0.5	18	melt	1.0	0.5	37.1	45.6	16.0	100.2	0.93	-	-
A1074	0.8	1200	22	22	melt	1.0	0.4	37.3	45.8	15.7	100.2	0.93	-	-
B596	0.8	1350	4	47	melt	1.0	0.4	37.1	45.6	16.2	100.3	0.94	-	-
A1171	1.3	1200	8	20	melt	1.1	0.5	36.6	45.7	16.1	99.9	0.95	-	-
B636	0.8	1175	8	18	melt	1.0	0.4	36.4	45.2	16.4	99.3	0.95	-	-
B600	0.8	1375	0.5	18	melt	1.0	0.5	37.1	45.6	16.0	100.2	0.93	-	-
A1074	0.8	1200	22	22	melt	1.0	0.4	37.3	45.8	15.7	100.2	0.93	-	-
B596	0.8	1350	4	47	melt	1.0	0.4	37.1	45.6	16.2	100.3	0.94	-	-
A1171	1.3	1200	8	20	melt	1.1	0.5	36.6	45.7	16.1	99.9	0.95	-	-
B589	1.3	1350	6	14	melt	1.0	0.3	36.9	45.6	16.6	100.5	0.95	-	-
B590	1.3	1375	12	16	melt	1.1	0.3	37.3	45.2	16.2	100.0	0.93	-	-
B591	1.3	1400	4	18	melt	1.1	0.5	37.4	45.8	15.8	100.6	0.92	-	-
B536	1.8	1300	24	9	melt	1.0	0.4	36.8	45.6	15.9	99.6	0.94	-	-
A1127	1.8	1450	12	17	melt	0.8	0.2	37.7	45.4	16.5	100.6	0.93	-	-

	P (GPa)	T (°C)	t (hrs)	n^a	Results	Cu	O	S	Fe	Ni	Total	M/S^b	F_{Fe}^{c}	F_{Ni}^{c}
						Chemical Composition (wt.%)								
B585	1.8	1425	4	21	melt	0.8	0.3	36.9	45.5	15.9	99.5	0.94	-	-
A1063	1.8	1400	4	49	melt	0.9	0.2	37.3	45.0	16.3	99.7	0.93	-	-
A1067	1.8	1350	18	8	melt	1.0	0.3	36.8	45.5	16.3	99.8	0.95	-	-
B601	1.8	1250	12	34	melt	1.0	0.4	37.9	45.4	15.8	100.3	0.91	-	-
A1162	1.8	1275	12	16	melt	1.0	0.3	36.9	45.6	16.6	100.5	0.95	-	-
B609	2.3	1275	2	12	melt	1.1	0.4	37.0	45.3	16.4	100.2	0.94	-	-
B594	2.3	1425	4	28	melt	1.0	0.3	37.5	45.1	16.0	99.8	0.92	-	-
B599	2.3	1400	4	19	melt	1.0	0.3	38.4	45.0	15.9	100.7	0.90	-	-
A1167	2.3	1300	6	30	melt	0.8	0.3	37.4	46.0	15.5	99.9	0.93	-	-
A1151	2.8	1450	4	10	melt	0.9	0.5	37.1	45.3	15.8	99.6	0.92	-	-
B615	2.8	1325	6	14	melt	0.9	0.5	36.4	45.0	16.4	99.2	0.94	-	-
A1122	2.8	1300	12	12	melt	1.0	0.4	36.0	45.3	16.7	99.4	0.97	-	-
A1153	2.8	1425	4	40	melt	1.2	0.4	36.9	45.0	15.9	99.5	0.93	-	-
A1163	2.8	1350	12	38	melt	1.0	0.6	36.7	45.1	16.2	99.7	0.93	-	-
A1160	3.3	1425	6	28	melt	1.0	0.3	38.0	45.3	16.2	100.8	0.91	-	-
A1152	3.3	1450	4	16	melt	1.0	0.4	37.6	45.2	16.3	100.5	0.92	-	-
A1161	3.3	1350	12	53	melt	1.0	0.5	37.0	45.2	16.2	100.0	0.93	-	-
A1159	3.3	1300	12	18	melt	1.1	0.3	37.3	45.2	16.2	100.0	0.93	-	-
A1180	3.3	1325	12	8	melt	0.9	0.6	37.4	44.6	16.1	99.7	0.90	-	-
M797	6.9	1425	2	10	melt	1.1	0.4	37.4	44.2	16.6	99.6	0.92	-	-
M796	7.95	1425	2	10	melt	1.0	0.4	36.4	45.8	16.4	100.0	0.96	-	-

Notes: a. Number of electron probe spot analyses averaged to obtain the reported elemental concentrations. b. Atomic metal/sulfur ratio, oxygen is regarded as replacing sulfur in mss or melts. c. Melt fractions (F) are calculated by mass balance of Fe and Ni according to $F = (C_{bulk} - C_{mss})/(C_{melt} - C_{mss})$, where C_{bulk} is the starting composition (C_{bulk} = 45.5 wt.% Fe or 16.2 wt.% Ni); C_{melt} is the concentration of Ni or Fe in the melt, and C_{mss} is the respective concentration in the crystalline phase.